ALUMINUM-LITHIUM ALLOYS: SURFACE-CRACKED TENSION FRACTURE TESTS AND PHYSICAL AND THERMAL PROPERTIES AT CRYOGENIC TEMPERATURES

P.T. Purtscher
M. Austin
S. Kim
D. Rule

ALUMINUM-LITHIUM ALLOYS: SURFACE-CRACKED TENSION FRACTURE TESTS AND PHYSICAL AND THERMAL PROPERTIES AT CRYOGENIC TEMPERATURES

P.T. Purtscher
M. Austin
S. Kim
D. Rule

Materials Reliability Division
Materials Science and Engineering Laboratory
National Institute of Standards and Technology
Boulder, Colorado 80303

March 1992

CONTENTS

ABSTRACT

Surface-cracked tension fracture tests were conducted in the T-S orientation at 295, 76, and 4 K on two plate alloys (X2095-T851, plate thickness of 12.7 mm and 2090-T81, plate thicknesses of 12.7 and 19.1 mm). The cryogenic toughness to room temperature toughness ratio for alloy 2090 is generally higher than that found for alloy X2095. Both alloys have significantly lower tensile properties near the surface of rolled plate than in the center of the plate.

The physical properties of seven plate specimens were measured from liquid helium to room temperature. Three variations in chemical composition of alloy X2095, three different samples of alloy 2090, and a single sample of alloy 2219-T87 were included. The mass density of Al alloys decreases by 4% / mass % of Li. The influence of texture on elastic properties is considered minimal because there is less than 5% variation in elastic-stiffness in the Al-Li alloys. The shear and Young's moduli increase 3 to 4% / mass % Li. The bulk modulus and Poisson ratio decrease by 3% / mass % Li.

Thermal expansion between 4 and 320 K was measured on the same seven plate specimens included in the physical properties study. All of the materials showed a typical temperature dependence where the slope of the coefficient of thermal expansion (CTE) vs. temperature curve has a zero slope near absolute zero and a smooth monotonic increase to a constant slope near room temperature.

The thermal conductivity of alloy X2095 (4%Cu-1%Li) was determined over the temperature range 4.2 to 300 K using a steady-state apparatus. The conductivity at 290 K was approximately 40% higher than at 77 K and was 37 times that at 4.6 K. The thermal conductivity of alloy X2095 is approximately twice that of alloy 2090, previously measured in the same apparatus. Compared to that of a published literature value for alloy 2219, the thermal conductivity of alloy X2095 is about 65% lower than for alloy 2219.

Keywords: aluminum-lithium alloys; cryogenic properties; elastic properties; fracture toughness; residual strength; thermal conductivity; thermal expansion

INTRODUCTION

The use of aluminum-lithium (Al-Li) alloys in this country has been hampered by the lack of engineering data, particularly at cryogenic temperatures [1]. Selected cryogenic mechanical properties of various high-strength Al-Li alloys have previously been measured and reported [2]. This report covers additional testing of Al-Li plates: (1) fracture tests of surface-cracked tension (SCT) panels, (2) measurement of physical properties including the elastic constants, mass densities and the elastic stiffness (a measure of texture), (3) thermal expansion, and (4) thermal conductivity. Measurement of specific heat will be performed by an outside contractor and will be included in a separate report. The test matrix is shown in Table 1. The chemical composition of the alloys is shown in Table 2.

All of the materials are 12.7 mm (0.5 in) thick with the exception of one plate of 2090 that is 19.1 mm (0.75 in) thick. Duplicate tests were run for elastic properties and thermal expansion from the center (19.1 mm thick-C) and from the near surface area (19.1 mm thick-S) of the thickest plate. Alloy 2219 is included as a baseline material that contains no Li.

This program is sponsored by the Air Force Systems Command, Phillips Laboratory, Edwards Air Force Base. It is part of the Materials and Processes Validation (3101) of the Structures, Materials, and Manufacturing (3000) portion of the Advanced Development Program for the National Launch System (NLS). The report is broken down into four separate sections that cover each type of test.

Table 1.   Test matrix for report.

material	elastic properties	thermal expansion	specific heat	SCT fracture	conduc-tivity
2090 12.7 mm	x	x		x	
2090-C 19.1 mm	x	x	x		
2090-S 19.1 mm	x	x		x	
X2095 lot 1	x	x			
X2095 lot 2	x	x		x	
X2095 lot 3	x	x	x		x
2219	x	x			

Table 2.   Chemical compositions of Al-Li and 2219 alloy plates.

Alloy	Cu	Li	Mg	Zr	Si	Fe	Ti	Ag	Ni
2090 12.7 mm	2.70	2.30	0.03	0.12	- -	0.08	0.19	- -	0.01
2090 19.1 mm	2.85	0.39	0.05	0.10	- -	0.02	0.13	- -	0.01
X2095 - lot 1	4.72	1.28	0.02	0.02	0.02	0.03	0.02	0.35	0.01
X2095 - lot 2	4.36	1.25	0.39	0.14	0.03	0.07	0.02	0.35	<0.01
X2095 - lot 3	4.08	1.01	0.35	0.13	0.03	0.03	0.03	0.35	- - -
2219	5.71	- - -	<0.0	0.15	0.07	0.02	0.03	- - -	<0.00

Section 1 -- SURFACE FLAW FRACTURE TESTING

Materials and Procedures

Three different Al-Li alloy plates were tested in this part of the program, X2095-T851 at a thickness of 12.7 mm (referred to as X2095) and 2090-T81 at two thicknesses of 12.7 and 19.1 mm (referred to as 2090-1/2 and 2090-3/4). These plates were part of an earlier test program and the initial characterization of the as-received plates can be found elsewhere [2]. The plate of X2095 used was previously identified as WL049-T851 lot 2, which contains 4.4% Cu and 1.3% Li.* Pertinent properties are summarized in Table 3. Data for alloy 2219-T87, currently used for the external tank of the space shuttle, are shown also for comparison. Fracture toughness ($K_{Ic}(J)$) decreased as the strength of the alloys went up. Alloy X2095 has the highest strength, but the lowest toughness of the three plates. The 2090-1/2 plate has a lowest strength, but the highest toughness, and properties of the 2090-3/4 plate are between the two extremes. Alloy 2219 has lower strength than the Al-Li alloys, and toughness and strength increase with decreasing temperature.

Table 3. Summary of previously reported mechanical properties (transverse orientation.

Alloy & Temp.	σ_y, MPa	σ_u, MPa	El., %	R.A., %	$K_{Ic}(J)$, MPa·$\sqrt{m}$
2090-1/2-295 K	507	546	2	4	32
- 76 K	570	610	1	4	39
- 4 K	621	669	1	4	46
2090-3/4-295 K	559	597	6	13	25
- 76 K	624	853	3	4	24
- 4 K	670	760	3	4	38
X2095 - 295 K	590	633	15	27	22
- 76K	670	760	9	15	22
- 4 K	775	853	9	14	22
2219 - 295 K	381	472	13	28	27
- 76 K	456	582	13	24	36
- 4 K	499	701	14	22	36

* Trade names are furnished to identify the materials and do not imple recommendation of endorsement by NIST.

3

Table 4 shows the initial plan for the SCT tests. The test program was designed so that the effects of material gage, specimen thickness (t), test temperature, flaw width (2c) and flaw depth (a) were examined. Stage 1 would look at the effect of temperature and material gage. Stage 2 would study the effects of temperature and flaw shape. Stage 3 would look at specimen thickness and test temperature. The starting plan was to obtain 6.4 mm thick sheets of both alloys 2090 and X2095 to test along with the 12.7 mm thick plates that were already on hand. The 6.4 mm thick sheets of alloys 2090 and X2095 could not be procured and additional tests on the materials already in hand were added to the program to finish in a timely fashion.

Table 4.   Test matrix for SCT tests for X2095 and 2090.

STAGE	295 K	76 K	4 K
I -- t=3.2 mm, a/c=0.25, a/t=0.7	2 from plate 2 from sheet	2 from plate 2 from sheet	2 from plate 2 from sheet
II -- t=3.2 mm, a/c=0.4, a/t=0.4	4 from plate	4 from plate	none
III -- t=2.2 mm,	3 from plate	3 from plate	none

The SCT fracture tests were conducted because the most likely mode of failure is the propogation of a crack through the thickness of the fuel tank. Previous tests [2] had characterized the in-plane orientations of the plate, but not the through-thickness orientation. All of the ADP participants attended a workshop held in Boulder, Colorado on July 31, 1990 and agreed that SCT tests were the most relevant to the design of the fuel tanks. The T-S orientation was chosen because it would give lower values than the L-S orientation.

The tests were conducted according to ASTM E 740-88 [3] for determining the residual strength of SCT specimens. Full-thickness, dog-bone shaped specimens were fatigue precracked at room temperature in three-point bending with a frequency of 25 to 35 Hz. A span of 127 mm was used for the bend fixture. Either electro-discharge machined slots or 0.60 mm diameter holes were used as starter notches for fatigue precracking. The precracking load varied from 17-2.5 kN for the 12.7 mm thick specimens to 45-4.5 kN for the 19.1 mm thick samples.

The supplemental analysis for fracture toughness is described in appendix X3.2 of ASTM E 740. The method uses the original crack dimensions to calculate the stress concentration factor and the residual strength as the critical load. The procedure is appropriate for low-toughness materials, where crack-tip plastic zones are small and stable crack growth prior to failure is absent. In all other cases, the fracture toughness analysis

4

is questionable and may lead to significant variations in toughness as the specimen and flaw dimensions change. In the test plan, stage 1 was designed so that the flaw and specimen dimensions would produce a valid toughness. The variations in flaw and specimen dimensions in stages 2 and 3 were such that a valid toughness may not be obtained. All of the data can be analyzed according to the empirical method described in section X3.4 of E 740, residual strength plotted against flaw size normalized to take into account the width of the crack and the thickness of the plate.

After a suitable fatigue crack was obtained, the specimens were machined to the test thickness over the complete gage length. The specimens were numbered so that the first digit refers to the stage of the test program, followed by a hyphen and a specimen number, see Table 5. Some specimens were machined from both sides so that the test section came from the center of the plate (these specimens have an * following the specimen identification), but most of the specimens were machined from one side so that the test section came from the near surface region of the plate. Figure 1 shows a schematic diagram that defines the various dimensions of the specimens. Figure 2 shows schematic diagram of the machining done after fatigue precracking to produce the final specimen dimensions for testing.

Flat tensile specimens (4 mm wide, 28 mm gage length, and with the same thickness as the SCT specimen) were taken from the gage section of the SCT specimen after SCT testing. Figure 3 is a schematic diagram illustrating the relative location of the tensile specimens in the SCT specimen. Tensile tests were performed at a constant cross-head rate of 0.05 cm/min.

The fracture surfaces of selected SCT specimens were observed in a scanning electron microscope (SEM) to document the failure mechanisms. The fracture surface observations are used to characterize the state of stress across the specimen thickness. Slant fracture, referred to as shear lips, is related to a state of plane stress while a flat fracture relates to plane strain. In the previous report [2], the superior toughness of alloy 2090-1/2 was attributed to numerous, large delaminations on the fracture surface that produced a state of plane stress. Alloy X2095 exhibited a flat fracture with few, small delaminations at cryogenic temperatures. The low toughness of alloy X2095 was then related to the stress state (plane strain) and the lack of delaminations on the fracture surface.

5
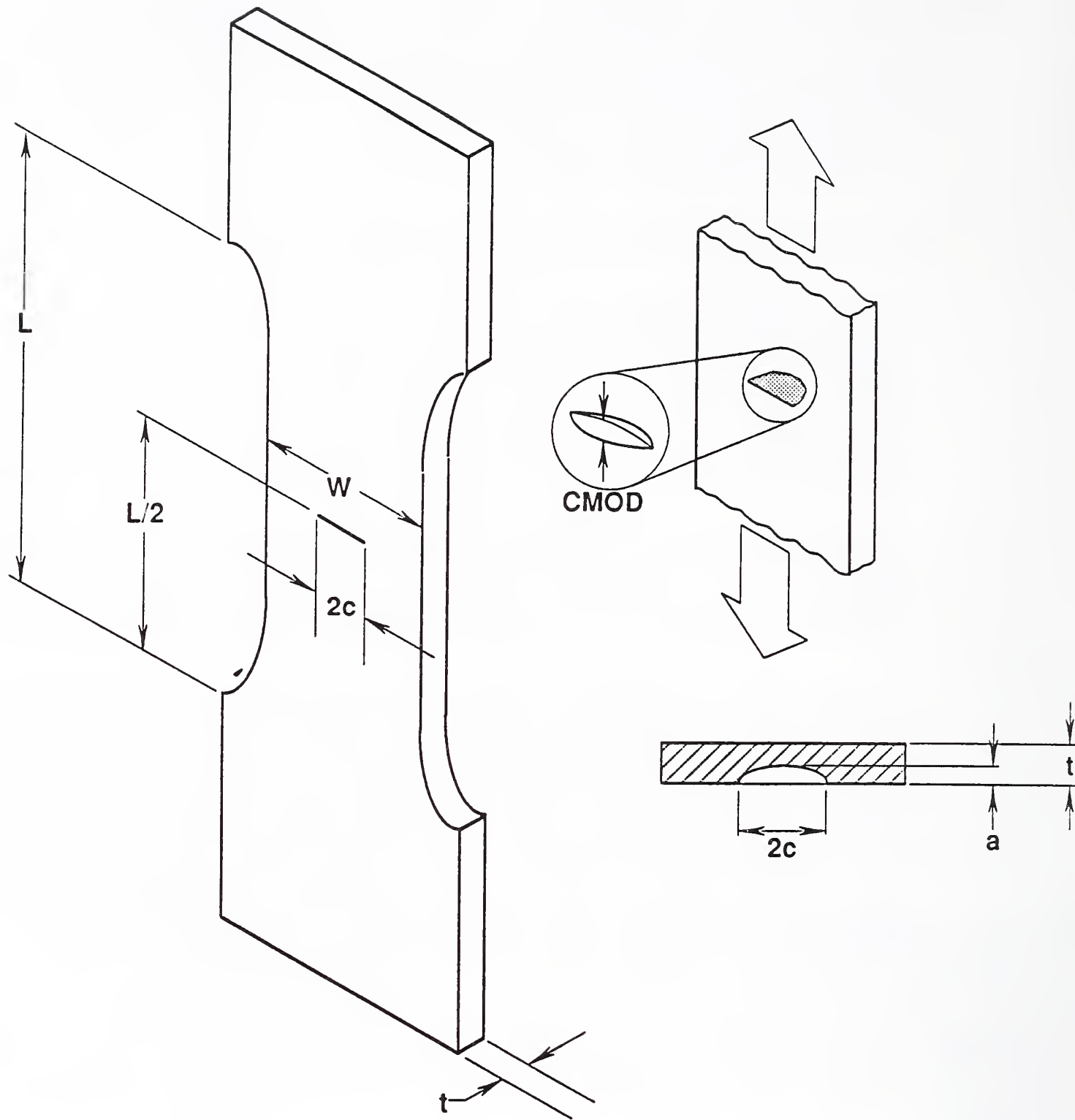
Fig. 1.   Schematic diagram showing the dog-bone shaped specimen
for the SCT test and all pertinent dimensions. For
these tests, L is 200 mm and W is 100 mm. The length
of the specimens, including the grips, is 450 mm.
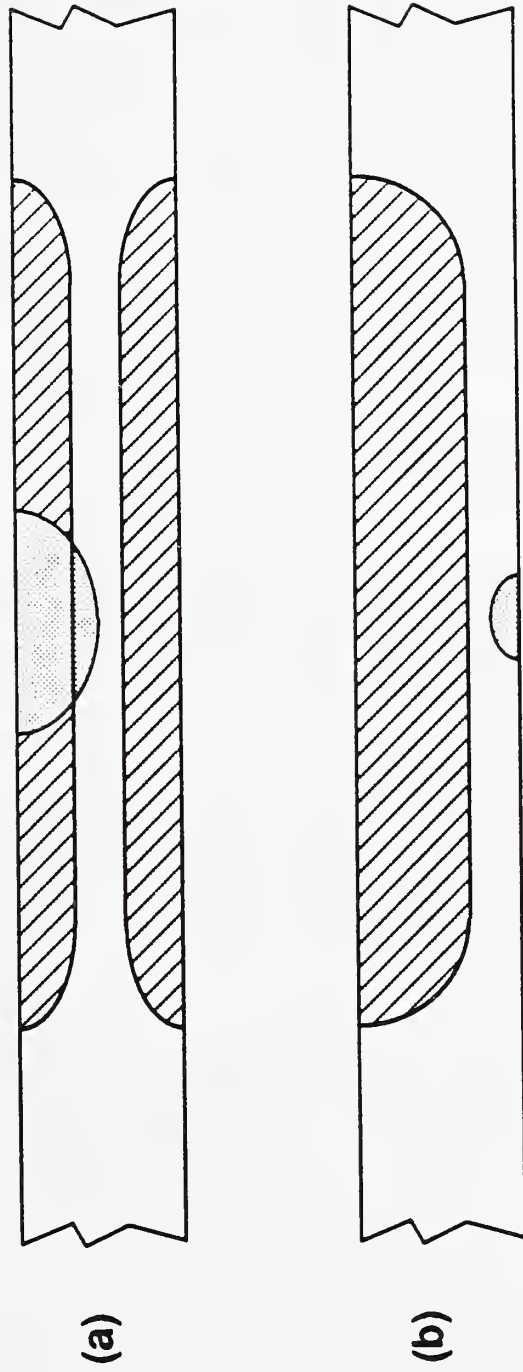
Fig. 2. Schematic diagram that shows the region of the specimen's cross section that was machined out after fatigue precracking (cross-hatched area) to produce the final thickness of the test specimen: (a) machined from center of plate and (b) machined from surface of plate. The fatigue precrack is represented by the fine dots.

Fig. 3.   Location where small, flat tension specimens were
           taken from the gage section of SCT specimen after SCT
           test.

Results

The SCT test results for alloy X2095 are summarized in Table 5. For alloys 2090-1/2 and -3/4, the results are shown in Tables 6 and 7. The specimen and flaw dimensions (a, t, and 2c) vary significantly as required in the test plan. The M/Φ and S values, the effective stress concentration factors, are defined in ASTM E 740. The residual strength (σ_R), thickness (t), and a/Φ^2 are the most significant columns to consider.

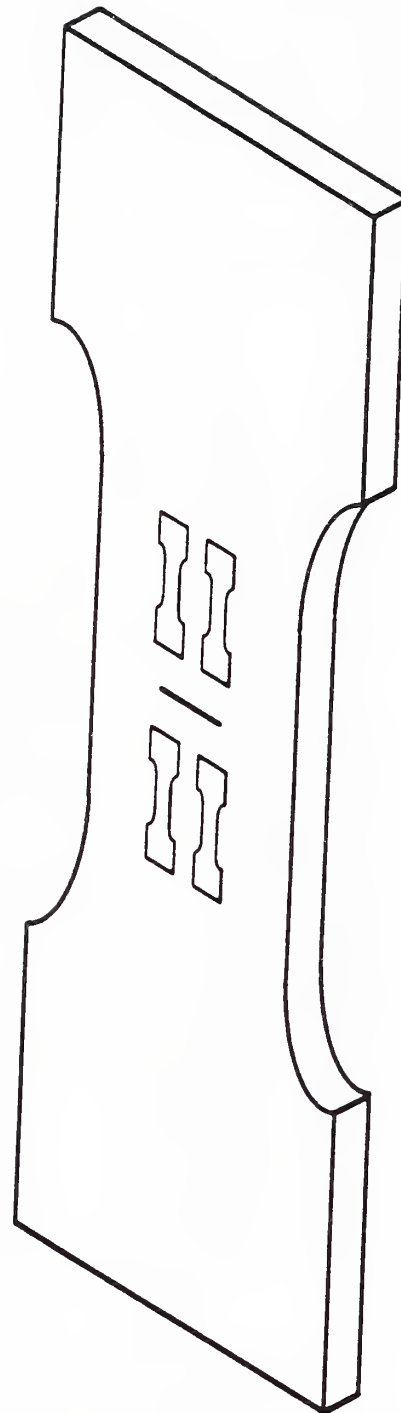The term $a/(\Phi^2 \cdot t)$ normalizes the data with respect to both the specimen thickness and flaw shape. A plot of residual strength for alloy X2095 vs. the normalized flaw size is shown in Fig. 4. The data at 295 K follow a trend where the residual strength decreases in a linear fashion as $a/(\Phi^2 \cdot t)$ increases. The data from stage 3 specimens, the thinnest specimens, fit the same trend as observed for stages 1 and 2. Two of these specimens were machined from the center and the others were machined from one side of the plate.

At 76 K, the data for alloy X2095 is generally lower than at 295 K (Fig. 4). For small flaws, $a/(\Phi^2 \cdot t) = 0.28$, there is large scatter. This variation is due to a change in fracture mechanism from plane σ for a shallow, wide crack to plane ϵ for a deeper, narrower crack. The observations that support this explanation are discussed later. The data at 4 K is limited, but the residual strength for a given flaw size appears higher than at 76 K, and about equal to the residual strength at 295 K.

The data for alloy 2090 from the two plates at 295, 76, and 4 K are plotted in Fig. 5. In general, the data for the two plates of 2090 at a given temperature are comparable. At a given flaw size, the 76-K residual strength is higher than the 295-K strength. The 4-K data are slightly higher than data at 76 K.

The tensile properties of SCT specimens are shown in Tables 8, 9, and 10. For alloy X2095 (Table 8), the flat tensiles taken from the mid-thickness of the plate have nearly the same strengths as the round specimens tested previously (shown in Table 3). The strengths at 76 K from flat tensiles measured near the surface are about 20% lower than in the mid-thickness of plates.

For alloy 2090-1/2 (Table 9), the flat tensiles taken from the mid-thickness of the plate were slightly stronger than the comparable round tensiles tested previously (Table 3). The strengths at 76 K of flat tensiles from the surface were about 12% lower than the properties of flat tensiles from the mid-thickness of the plate. For alloy 2090-3/4 (Table 10), flat tensiles machined from the surface of the plate exhibited 10 to 15% lower strengths than found in round specimens machined from the mid-thickness of the plates (Table 3). The tensile ductilities of all the flat tensiles from alloy 2090 were extremely low.

9

Table 5. Summary of SCT panels tests on alloy X2095 (WL049).

spec. #	a (mm)	t (mm)	2c (mm)	M/Φ	a/Φ² (mm)	S	σ_R (MPa)	K_Ie (MPa·√m)
tested at 295 K								
1-3	1.92	3.23	22.6	1.64	2.21	0.50	352	44
1-12	1.72	3.36	16.4	1.42	1.77	0.55	449	47
2-5	1.77	3.18	5.23	0.89	1.00	1.00	524	- - -
2-8	2.05	3.21	6.97	1.00	1.28	0.95	476	- - -
2-12	1.51	3.41	6.85	1.06	1.10	0.78	504	- - -
3-1	0.95	2.36	4.05	1.01	0.67	0.79	518	- - -
3-4	2.44	3.26	8.28	1.03	1.51	0.99	449	- - -
3-29	0.95	2.51	3.79	1.10	0.65	0.85	495	- - -
3-5	2.13	2.87	10.8	1.30	1.62	0.81	384	- - -
tested at 76 K								
1-11	1.77	3.33	17.6	1.45	1.56	0.53	387	41
1-4	2.36	3.28	26.1	1.81	2.18	0.54	276	43
2-1	2.49	3.10	4.28	0.63	0.87	1.42	407	- - -
2-3	3.08	3.56	6.72	0.77	1.36	1.33	345	- - -
2-4	2.87	3.56	5.54	0.70	1.13	1.38	435	- - -
2-7	2.26	3.15	6.15	0.88	1.21	1.08	393	- - -
2-9	1.79	3.18	7.46	1.07	1.26	0.84	400	- - -
2-10	1.59	3.13	7.26	1.08	1.15	0.78	455	- - -
2-11	1.23	3.21	5.51	1.01	0.90	0.77	607	- - -
3-3	2.46	2.81	10.0	1.19	1.69	0.96	340	- - -
3-2	2.13	2.36	6.41	0.98	1.23	1.13	345	- - -
3-30	1.23	2.05	5.15	0.98	0.65	0.81	418	- - -
tested at 4 K								
1-10	2.13	3.41	20.9	1.59	1.92	0.56	317	42
1-13	1.33	2.95	16.7	1.44	1.26	0.47	531	50

Table 6. Summary of SCT panels tests on alloy 2090-1/2.

spec.#	a (mm)	t (mm)	2c (mm)	M/Φ	a/Φ² (mm)	S	σ_R (MPa)	K_{Ie} (MPa·√m)
tested at 295 K								
1-1*	2.51	3.49	21.2	1.61	2.21	0.62	338	48
2-31	0.82	3.23	19.2	1.28	0.80	0.33	386	- -
1-35	2.59	3.13	15.0	1.48	2.10	0.77	352	47
1-15*	2.03	3.18	16.3	1.49	1.77	0.62	345	41
tested at 76 K								
1-5*	1.51	3.26	13.5	1.34	1.36	0.55	449	41
1-14*	1.31	3.26	22.7	1.46	1.26	0.55	400	37
1-33	2.31	3.15	18.0	1.57	2.00	0.65	381	51
2-32	1.49	3.08	7.82	1.14	1.15	0.73	446	- -
2-2	2.08	3.46	4.95	0.79	1.00	1.12	455+	- -
tested at 4 K								
1-9*	1.77	3.54	10.1	1.19	1.41	0.70	545	48
1-34	1.46	3.13	15.0	1.39	1.33	0.52	512	48
1-16*	1.72	3.13	20.3	1.57	1.59	0.50	518	59

11

Table 7. Summary of SCT panels tests on alloy 2090-3/4.

spec.#	a (mm)	t (mm)	2c (mm)	M/Φ	a/Φ^2 (mm)	S	σ_R (MPa)	K_{Ie} (MPa·$\sqrt{m}$)
tested at 295 K								
2-13	0.62	3.18	11.1	1.18	0.59	0.37	501	26
2-16	1.21	3.38	10.9	1.23	1.07	0.54	378	26
2-16	1.18	3.18	3.38	0.84	0.65	0.88	489	32
2-21	2.05	3.18	8.38	1.18	1.41	0.87	359	32
3-26	0.44	2.28	3.03	1.04	0.37	0.60	548	--
3-22	0.90	2.33	5.69	1.15	0.74	0.65	474	--
tested at 76 K								
2-16	2.18	3.28	15.7	1.45	0.85	0.60	363	--
2-20	1.49	3.36	5.23	0.95	0.94	0.88	512	--
2-27	0.87	3.18	4.79	1.04	0.68	0.60	545	--
3-25	1.31	2.33	4.77	1.01	0.85	0.90	436	--
3-26	0.69	2.28	8.56	1.24	0.65	0.46	527	--
3-17	0.85	2.31	9.15	1.28	0.78	0.46	418	--
2-18	1.51	3.21	10.7	1.26	1.28	0.63	489	40
tested at 4 K								
1-15	1.62	3.21	10.2	1.24	1.33	0.67	482	42
1-23	0.97	3.28	12.2	1.24	0.91	0.45	596	41
3-36	1.77	2.18	12.9	1.60	1.51	0.70	360	47

NORMALIZED FLAW/THICKNESS

RESIDUAL STRENGTH, MPa
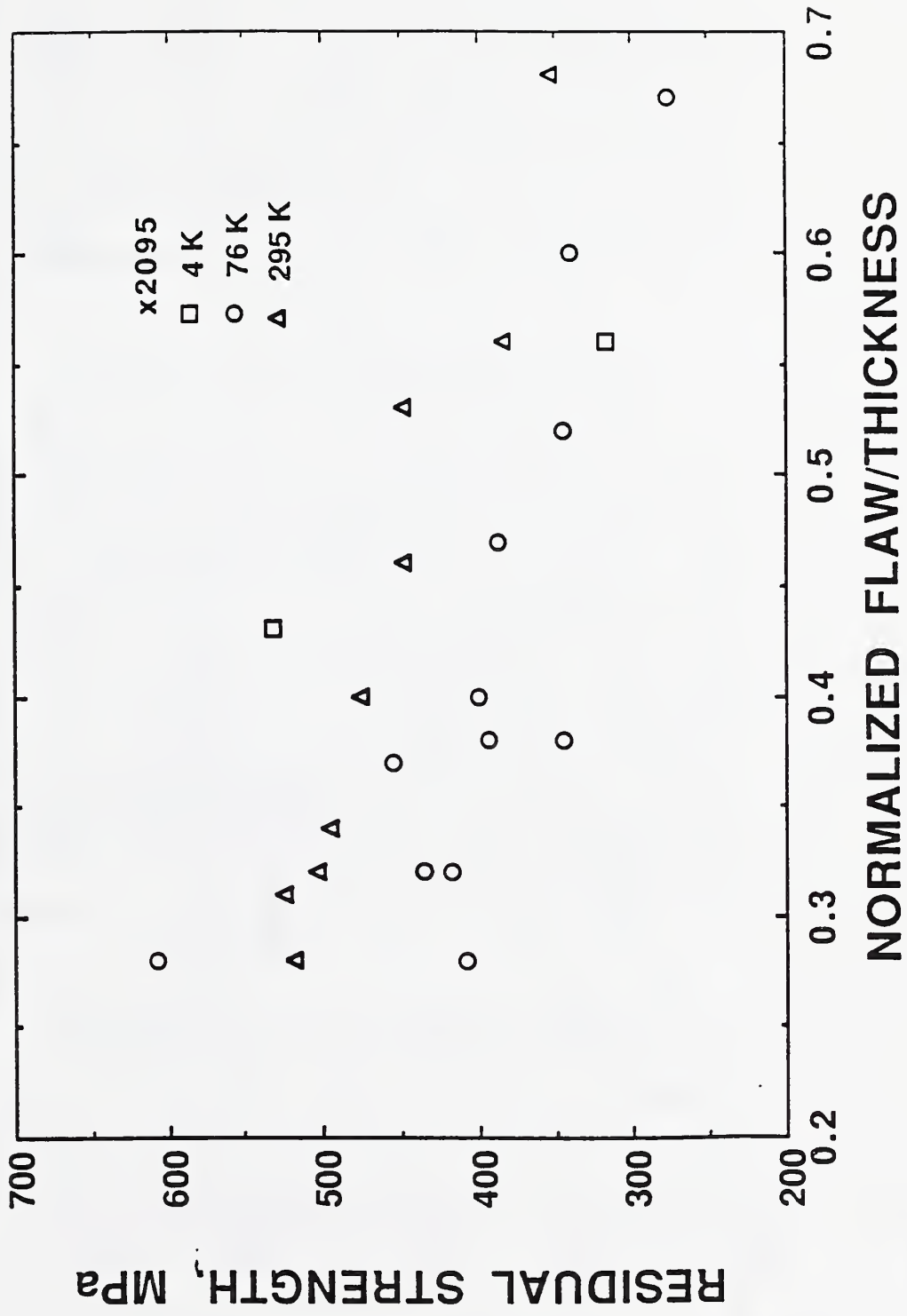
x2095
□ 4 K
○ 76 K
△ 295 K

13

Fig. 4.   Residual strength vs. normalized flaw size per unit thickness for alloy X2095-T851 (lot 2) plate at the three test temperatures.
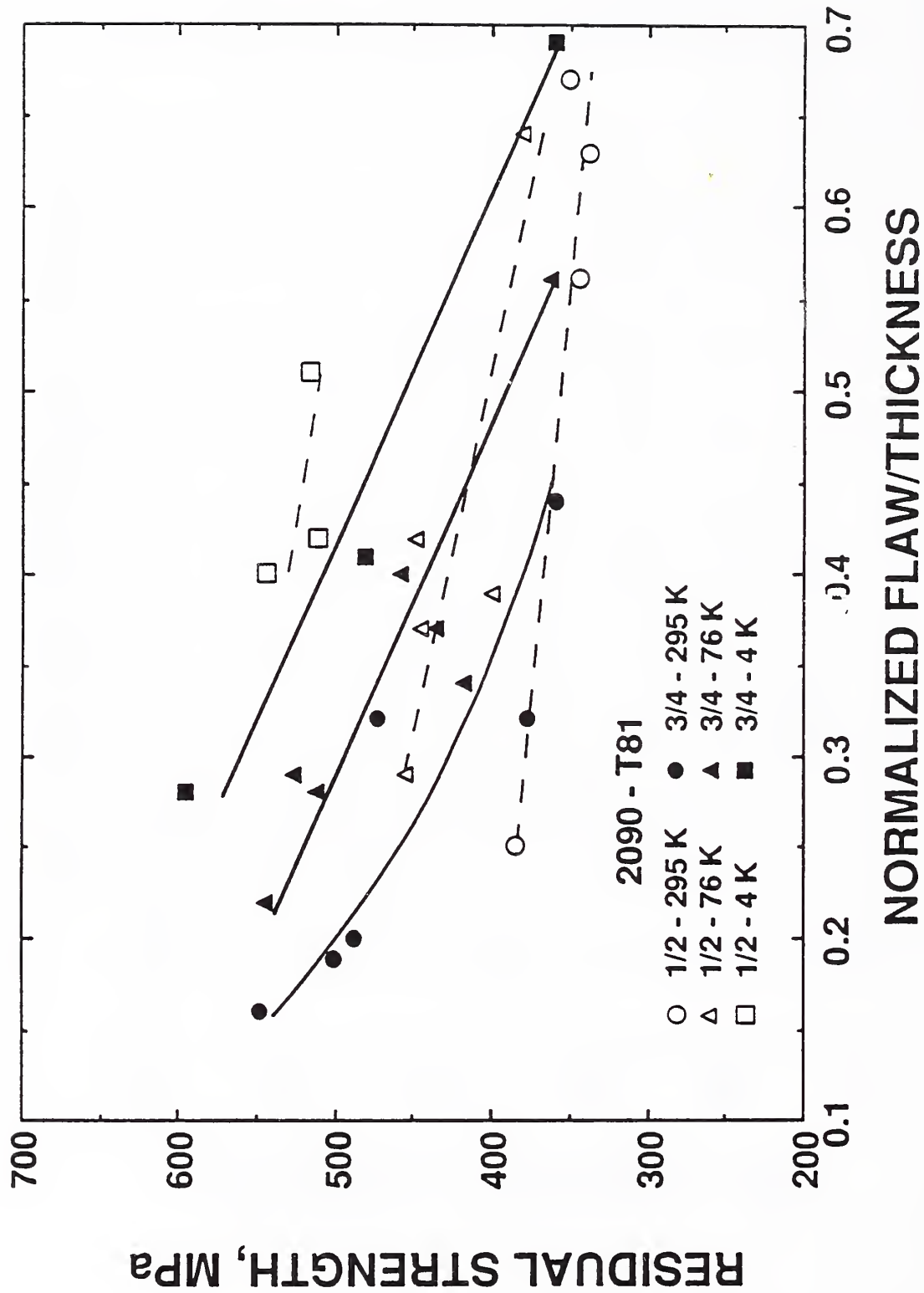
Fig. 5. Residual strength vs. the normalized flaw size per unit thickness for alloy 2090-T81 -1/2 and -3/4 plates at the three test temperatures. The dashed lines are for 2090-1/2 while the solid lines are for 2090-3/4.

Table 8.   Summary of tensile properties of flat
            tensiles taken from X2095 SCT specimens.

Temperature	YS, MPa	UTS, MPa	El., %
from center			
295 K	589	618	4
76 K	718	773	●.5
4 K	749	828	●.5
from surface			
76 K	566	631	7.5

Table 9.   Summary of tensile properties of flat
            tensiles taken from 2090-1/2 SCT specimens.

Temperature	YS, MPa	UTS, MPa	El., %
machined from center			
295 K	531	552	0.7
76 K	607	621	0.5
4 K	649	690	1.5
machined from surface			
76 K	538	538	0.2

Table 10.   Summary of tensile properties of flat
             tensiles taken from 2090-3/4 SCT specimens.

Temperature	YS, MPa	UTS, MPa	El., %
machined from surface			
295 K	507	533	1.7
76 K	555	589	1.4

15

Large shear lips are evident on fracture surfaces of specimens from alloy X2095 tested at 295 K when observed in the SEM, indicating that there was a large plane σ component to the stress state at that temperature. In general, the size of the shear lips decreases as the test temperature decreases. At cryogenic temperatures, the fracture appearance of X2095 specimens depended on the flaw shape. Flaws with a lower a/c ratio show larger shear lips.

The influence of a/c ratio on the size of the shear lips is illustrated in Fig. 6 by comparing the appearance of specimens 2-1 and 2-11, both X2095 specimens tested at 76 K and with nearly the same value of $a/\Phi^2/t$. For the deeper and narrower crack (specimen 2-1), the first increment of crack growth along the surface of the specimen from the fatigue crack has smaller shear lips. The shear lip remains a constant width of 0.1 mm for approximately 2 mm along the surface before the width of the shear lips increased to about 0.4 mm. These observations can be taken as proof that there was 2 mm of stable crack growth along the free surface before final fracture. For the shallower, wider crack (#2-11), larger shear lips form adjacent to the fatigue precrack. These observations indicate that there was no slow, stable crack growth prior to final fracture in specimen 2-11.

For the 2090-3/4 plate, a representative specimen tested at 76 K is shown in Fig. 7. The fracture surface exhibits small delaminations with little out-of-plane cracking, 0.5 to 1 mm. Specimens tested at 295 K show the same small delaminations with occasional out-of-plane cracking, on the order of 1 to 2 mm.

Specimens from the 2090-1/2 plate usually have more out-of-plane cracking and delaminations than the thicker plate, 2090-3/4. Figure 8 shows the fracture surface from one specimen of the 2090-1/2 plate tested 76 K. The delaminations in the specimen are approximately equal to the grain size, which are mostly large and not recrystallized. In the 2090-3/4 plate, the grains were smaller and recrystallized. The grain structure of each material was shown in the previous report [2].

Discussion

An important consideration in choosing the material for cryogenic fuel tanks is the ratio of material properties (yield strength and fracture toughness) at room temperature (295 K) where the tank is proof tested and the operating temperature [4]. The ideal material would show an increase in toughness commensurate with the increase in yield strength that accompanies the lower service temperature, similar to the properties of alloy 2219 found in Table 3. The yield strength and toughness ratios for the three plates of Al-Li alloys tested in this program are shown in Table 11. The toughness ratio for the 2090 plates are significantly higher than the ratio for alloy X2095. The reason for this is the relatively low toughness of the 2090 plates at 295 K, rather than high toughness of alloy 2090 at cryogenic temperature. This point is emphasized by looking at the residual strength as a function of normalized flaw size for all three plates at liquid nitrogen temperature

16

0.5 mm

slow crack growth →

B →

A

17

Fig. 6. (a) SEM fractograph of the fracture surface of alloy X2095, specimen #2-1 that was tested at 76 K, showing the starter notch (drill holes), fatigue precrack (dark, hemispherical area), region of slow crack growth (marked along bottom edge), and the change in shear lip size from stable (labeled A) to unstable (labeled B) crack growth.

0.5 mm

B

Fig. 6. (b) SEM fracograph of the fracture surface of alloy X2095, specimen #2-11 that was tested at 76 K, showing the fatigue precrack and a relatively uniform shear lip (labeled B) due to unstable crack growth.

18

0.5 mm

Fig. 7.   SEM fractograph of the fracture surface of alloy 2090-3/4, tested at 76 K, showing part of the fatigue precrack and the initial crack growth.

19

0.5 mm

20

Fig. 8.   SEM fractograph of the fracture surface of alloy 2090-1/2, tested at 76 K, showing part of the fatigue precrack and the initial crack growth.

Table 11.   Summary of mechanical property ratios
            calculated for Al-Li alloys.

alloy plate	$\dfrac{YS(76\ K)}{YS(295\ K)}$	$\dfrac{YS(4\ K)}{YS(295\ K)}$	$\dfrac{K_{Ie}(76\ K)}{K_{Ie}(295\ K)}$	$\dfrac{K_{Ie}(4\ K)}{K_{Ie}(295\ K)}$
2090-1/2	1.14	1.22	0.95	1.14
2090-3/4	1.09	- - - -	1.36	1.36
X2095	1.22	1.27	0.92	1.01

shown in Fig. 9. There is little difference between the three except for the
smallest normalized flaws where the residual strength of X2095 depends
critically upon the flaw shape, as discussed in the results section.

There are three possible fracture modes for an SCT specimen. First, the
specimen can fail under plane strain conditions, like the compact tension
specimens tested previously. Plane strain conditions represent the theoret-
ical minimum residual strength for a given flaw size, and the toughness should
be equal to $K_{Ic}(J)$. The second possible fracture mode is plane stress. In
this stress state, the toughness and residual strength are always higher than
in plane strain and depends upon the specimen thickness and yield strength.
The maximum residual strength in plane stress conditions would be for the case
where the material fails by general yielding of the section. Cheng et al. [5]
describe a procedure for predicting the maximum stress σ_{max} where the net
section yields and their equation is shown below

$$\sigma_{max} = \sigma_{eq}\{1-[(a \cdot 2c)/(t \cdot W)]\}, \tag{1}$$

where σ_{eq} is the average of the yield and ultimate strengths measured in the
tensile tests, a and 2c are the dimensions of the surface crack, and t and W
are the thickness and width of the specimen's gage section. The value of σ_{max}
calculated in this way would be equal to the residual strength of the specimen
under general yielding conditions.

The results for alloy X2095 at 76 K can be used as an example of how the
failure mode affects the measured residual strength. Figure 10 shows the
measured data with respect to the maximum and minimum predicted residual
strength. A simulated flaw, which increases with a constant a/c ratio of 0.2,
is used to calculate the residual strength for the two extremes of plane
strain and general yielding. Most of our data fall between the two extremes,
but closer to the plane strain value. The exception is for the shallow, wide
flaw discussed previously where the residual strength is actually slightly
higher than theory predicts. At the smallest flaw sizes, the theoretical
plane strain failure yields higher predicted residual strength than found for
general yielding, indicating that the tensile properties of the material will
limit the residual strength of a material as the flaw size is decreased.
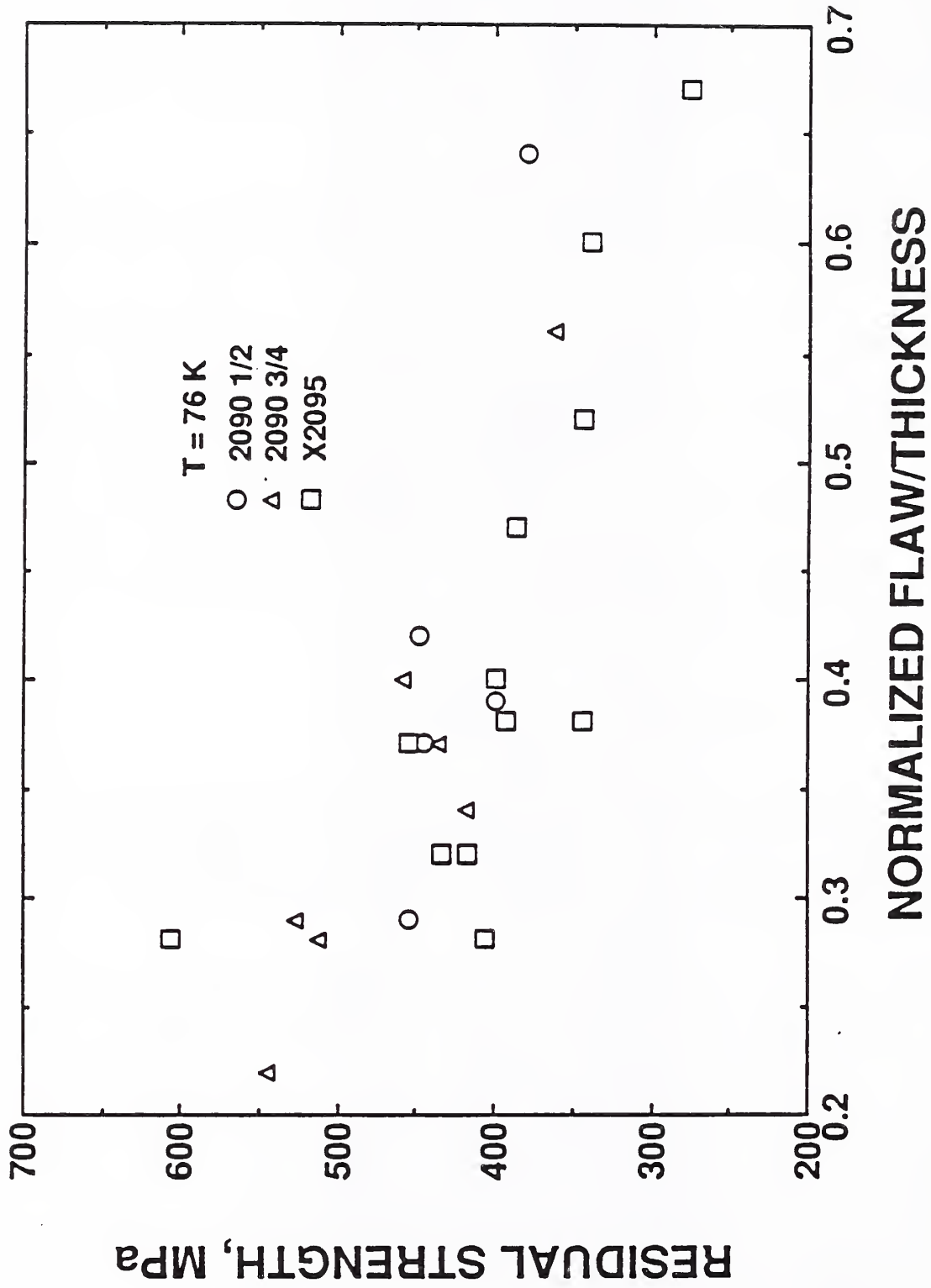
21

Fig. 9.   Residual strength vs. normalized flaw size per unit thickness for both alloys, 2090 and X2095 at 76 K.
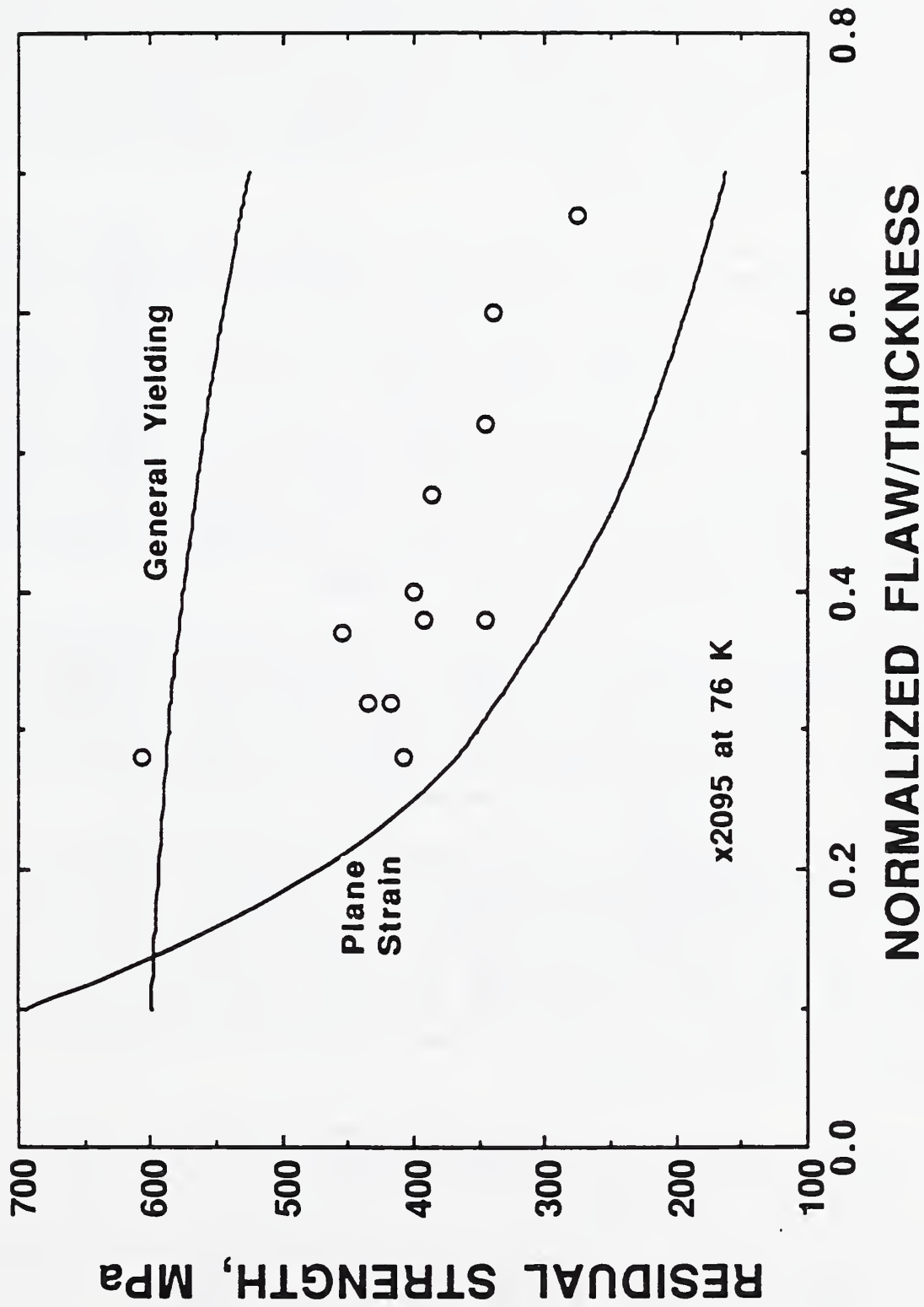
Fig. 10. Residual strength vs. normalized flaw size per unit thickness for alloy X2095 at 76 K along with the predicted failure loads for two possible failure criteria, general yielding and plane strain.

The data generated in this test program can be compared to previously reported data [4,6]. The data for alloy X2095 tested at 76 K are shown in Fig. 11. The two tests from [4] are at a relatively small flaw size, and compare favorably to the one test from this program where the specimen failed by general yielding. For alloy 2090, the two tests in [6] and a single test in [4] are shown in Fig. 12 along with our data. Again, there appears to be some agreement between tests from the different sources.

The two Al-Li alloys tested in this program behave in quite different ways in the SCT test. Alloy X2095 behaves like an isotropic material with no appreciable delaminations. Changes in fracture mode from plane stress to plane strain are possible and need to be considered in the design and testing of the alloy. The ratio of toughness at cryogenic temperatures to room temperature is not greater than 1 so that the high tensile strength may not be useable in design and proof test.

Alloy 2090 fails by the linking up of intergranular delaminations, and its properties depend critically upon the orientation with respect to the rolling direction. In the T-S orientation used in this program, the delaminations deflect the fatigue crack, lowering the local stress concentration. The two plates of 2090 tested in this program are significantly different in grain structure and size of the delaminations, yet the residual strength and toughness values for the two were remarkably similar. In either case, the delaminations seem to produce plane stress fracture over a wide range of flaw and specimen dimensions. Even the fatigue crack grows along delaminated grain boundaries, so the flat fracture surface is not observed in this alloy. Differences between the two plates of 2090 in tensile properties and grain structure are not reflected in residual strength.

A difference in strength between the surface and mid-thickness of the plates is observed in both Al-Li alloys. This difference could be due to a change in the cryostallographic texture from surface to mid-thickness. A similar effect was found previously [2] where the tensile properties at the mid-thickness for round specimen oriented at 45° to the rolling direction were less than the longitudinal or transverse tensile properties.

Overall, the results of the SCT testing have shown that the two Al-Li alloys fail by different mechanisms, but have similar strength and toughness properties. Alloy 2090 generally has a better toughness ratio than alloy X2095, but not as consistent as previously found in alloy 2219. The results also show that the tensile properties can vary significantly, depending upon the location through the thickness of the plate. Clearly, flat tensiles taken from the gage section of the SCT specimens are needed to correlate tensile properties to fracture properties.

The results have not provided a clear understanding of the relationship between tensile properties and fracture properties. Future testing should include alloy 2219 for comparison, so that the influence of tensile properties, delaminations, and alloy composition can be evaluated better. A quantitative evaluation of texture that relates directly to the tensile properties would help to sort out variations in the materials and could aid in the inspection of as-received plates.

24

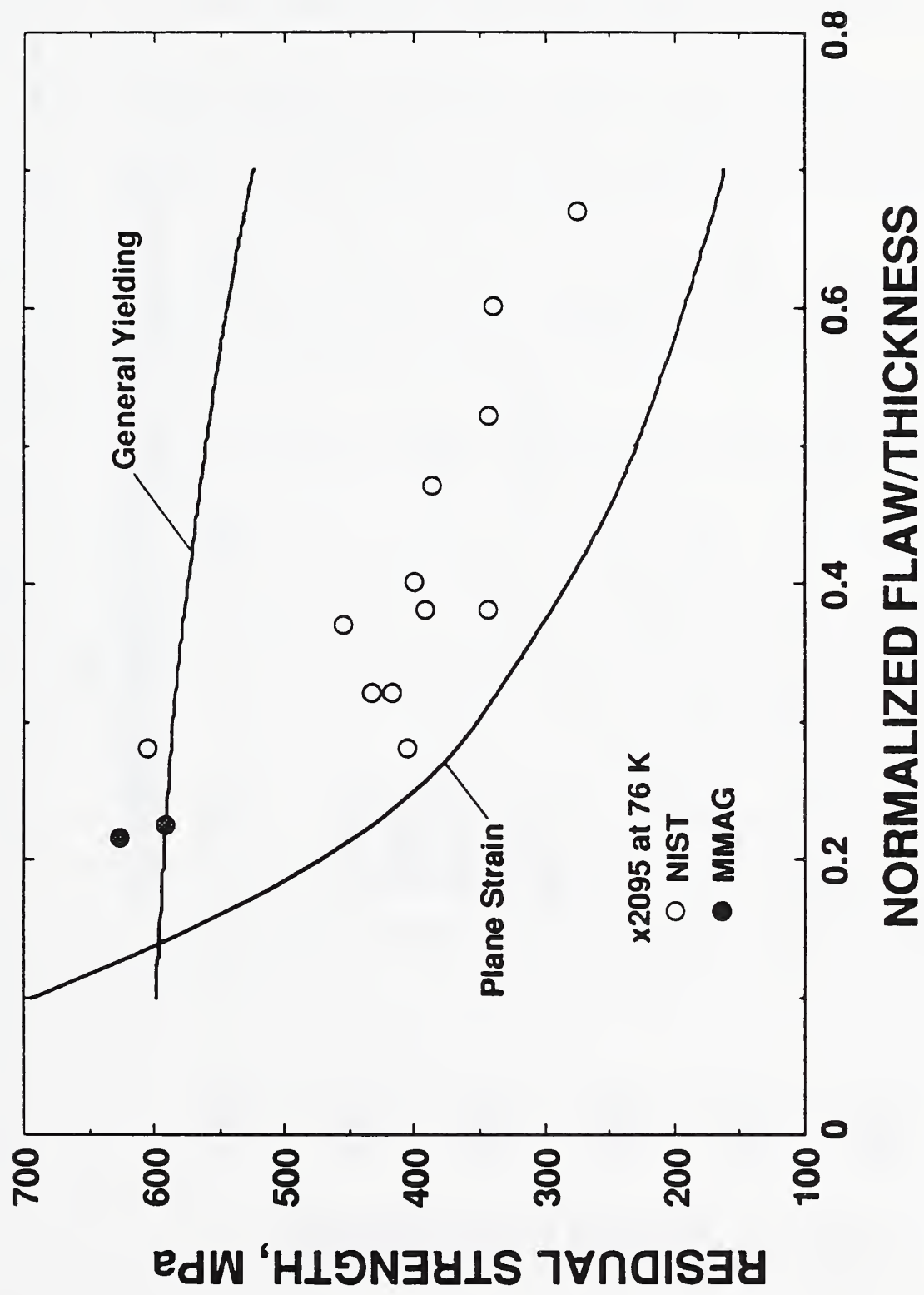Fig. 11. Same as Fig. 10 but with data from [4] added.

NORMALIZED FLAW/THICKNESS
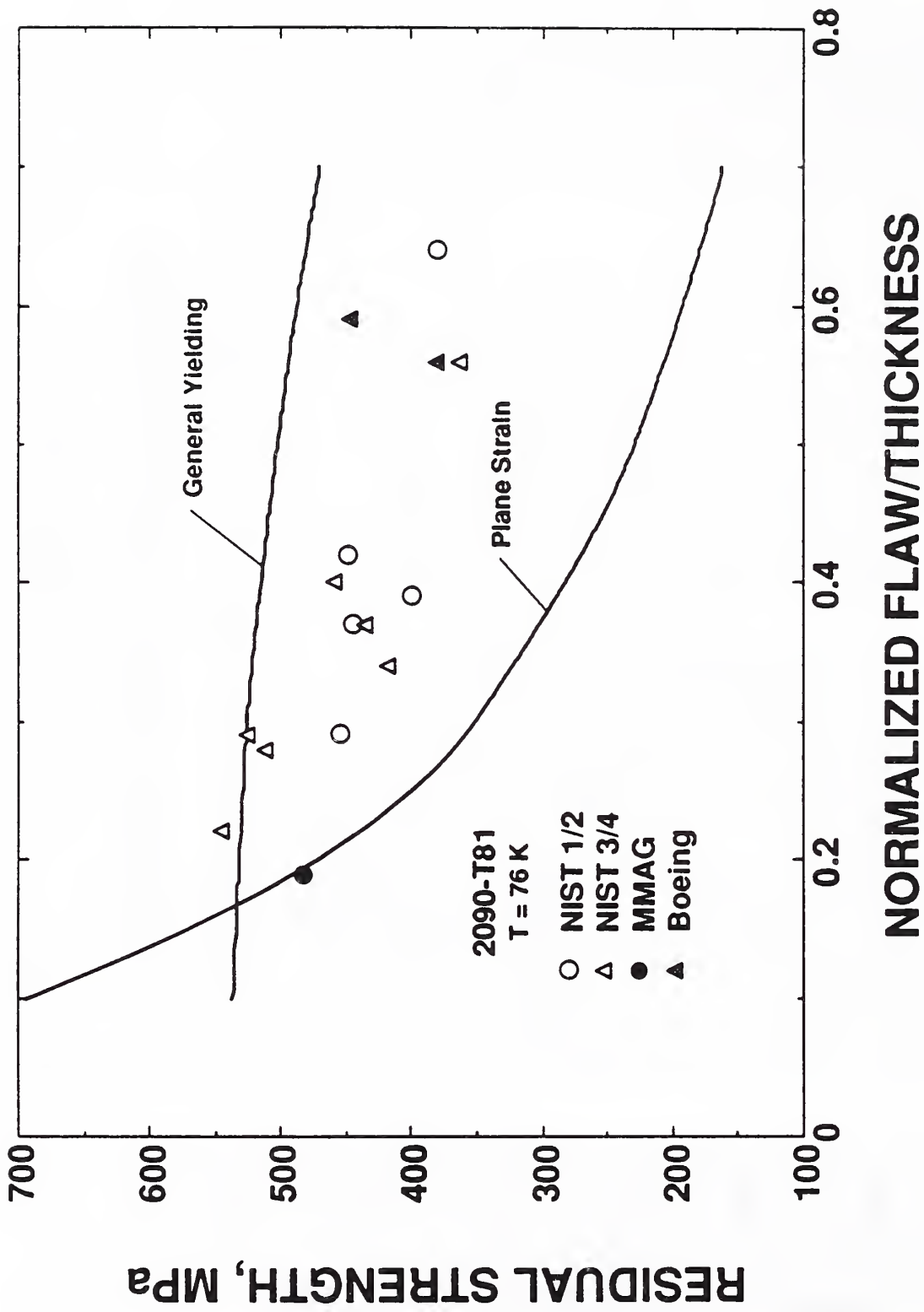
RESIDUAL STRENGTH, MPa

Fig. 12. Residual strength vs. normalized flaw size per unit thickness for alloy 2090 at 76 K showing data from three sources: this report, [6], and [4].

26

Conclusions

1.   The residual strength of SCT specimens of both alloys decreases as the flaw size increases. The ratio of cryogenic toughness to room temperature toughness for alloy 2090 is generally higher than that found for alloy X2095. The ratio of yield strengths (cryogenic to room temperature) is higher for alloy X2095 than for alloy 2090.

2.   The residual strength for alloy X2095 at cryogenic temperatures depends critically upon the stress state for the initial crack growth. If the crack grows under plane strain rather than plane stress, the residual strength will be lower. Flaw shape determines the state of stress for the initial crack growth.

3.   The residual strength of alloy 2090 did not vary significantly for the two plates tested in this program. The low tensile ductility of these materials did not translate into poor residual strength.

4.   Both alloys have significantly lower tensile strengths near the surface of the plate than in the center of the plate.

Section 2 -- ELASTIC PROPERTIES

Elastic-constant Measurement Methods

We used a megahertz-frequency pulse-echo-superposition method to determine the elastic stiffnesses C using the general relationship

$$C = \rho v^2. \tag{2}$$

Here, ρ denotes mass density and v denotes sound velocity.

For mass density, we used Archimedes's method with distilled water as a standard. We estimate the inaccuracy as 0.05%. Sound velocity was measured by a megahertz-frequency pulse-echo-superposition method. Quartz transducers were bonded to the specimens with phenyl salicylate for room-temperature measurements and with a Celvacene-light for lower temperatures. Failure of these bonds at very low temperatures required using a dimethyl polysiloxane (silicone fluid with viscosity = 2 x 10^4 Pa·s at 25°C) or ethanol for bonding. The specimen holder was placed in a dynamic gas-exchange cryostat, and temperature was varied using liquid helium. Temperatures were monitored with a temperature controller using two gold-iron/chromel 0.07% thermocouples, one in the specimen holder and another in the gas chamber.

Measurements were performed on seven different specimens shown in Table 1. The chemical composition of each specimen was included in Table 2. For each of the seven specimens, we measured nine sound velocities corresponding to the longitudinal elastic constants C_{11}, C_{22}, C_{33} and the transverse elastic constants $C_{44}(C_{3232}$ and $C_{2323})$, $C_{55}(C_{1313}$ and $C_{3131})$, $C_{66}(C_{1212}$ and $C_{2121})$. For sound velocities, we estimate a 0.2% inaccuracy. Thus we estimate less than 0.5% error in elastic constants.

Results

The study's principal results are reported in Table 12. The table shows mass densities, elastic constants, and Poisson ratios at ambient temperature. We calculated longitudinal modulus C_1 and shear modulus G from the arithmetic average of the longitudinal and transverse elastic constants. All other elastic constants that describe polycrystalline aggregates relate simply to these two moduli:

$$Young\ modulus \equiv E = \frac{G(3C_1 - 4G)}{C_1 - G} \quad, \tag{3}$$

28

Section 2 -- ELASTIC PROPERTIES

Elastic-constant Measurement Methods

We used a megahertz-frequency pulse-echo-superposition method to determine the elastic stiffnesses C using the general relationship

$$C = \rho v^2. \tag{2}$$

Here, ρ denotes mass density and v denotes sound velocity.

For mass density, we used Archimedes's method with distilled water as a standard. We estimate the inaccuracy as 0.05%. Sound velocity was measured by a megahertz-frequency pulse-echo-superposition method. Quartz transducers were bonded to the specimens with phenyl salicylate for room-temperature measurements and with a Celvacene-light for lower temperatures. Failure of these bonds at very low temperatures required using a dimethyl polysiloxane (silicone fluid with viscosity = 2×10^4 Pa·s at 25°C) or ethanol for bonding. The specimen holder was placed in a dynamic gas-exchange cryostat, and temperature was varied using liquid helium. Temperatures were monitored with a temperature controller using two gold-iron/chromel 0.07% thermocouples, one in the specimen holder and another in the gas chamber.

Measurements were performed on seven different specimens shown in Table 1. The chemical composition of each specimen was included in Table 2. For each of the seven specimens, we measured nine sound velocities corresponding to the longitudinal elastic constants C_{11}, C_{22}, C_{33} and the transverse elastic constants $C_{44}(C_{3232}$ and $C_{2323})$, $C_{55}(C_{1313}$ and $C_{3131})$, $C_{66}(C_{1212}$ and $C_{2121})$. For sound velocities, we estimate a 0.2% inaccuracy. Thus we estimate less than 0.5% error in elastic constants.

Results

The study's principal results are reported in Table 12. The table shows mass densities, elastic constants, and Poisson ratios at ambient temperature. We calculated longitudinal modulus C_1 and shear modulus G from the arithmetic average of the longitudinal and transverse elastic constants. All other elastic constants that describe polycrystalline aggregates relate simply to these two moduli:

$$Young\ modulus \equiv E = \frac{G(3C_1 - 4G)}{C_1 - G}\ , \tag{3}$$

28

$$Bulk\ modulus \equiv B = C_l - \frac{4}{3}G \ , \tag{4}$$

$$Poisson\ ratio \equiv \nu = \frac{(C_l - 2G)}{2(C_l - G)} \ . \tag{5}$$

The elastic constants obtained from these relationships are shown as functions of temperature in Fig. 13 for the specimen taken from the center of 2090-3/4. This trend is representative of all the specimens. The elastic constants at selected temperatures are given in Appendix A. The temperature dependences were fitted to a theoretical relationship [7]:

$$C(T) = C(0) + \frac{s}{e^{t/T} - 1} \ . \tag{6}$$

Here, C(T) denotes elastic stiffness in GPa; C(0) and s with units of GPa and t with units of K are parameters that can be related to simple atomic models. Appendix A also gives those parameters determined from a least squares fit.

Discussion and Summary

As shown in Table 12, the mass density shows remarkable variation: approximately 4% change per mass % Li. It is not surprising because lithium is the lightest metallic element. Table 12 shows also that texture in these alloys appears to be not too significant with respect to elastic constants. In pure aluminum, texture can cause directional elastic-stiffness variation of up to 20%. Table 12 shows a maximum variation of 4.5%.

Lithium's alloying effect on the elastic constants can not be accurately determined from this study because of the large number of other elements and their interactions. However, our results show that shear and Young moduli increase with lithium content (increase 3 to 4% per mass % Li), while the bulk modulus and Poisson's ratio decrease (decrease 3% per mass % Li).

All of the elastic moduli increase with decreasing temperature, achieve zero slope near T = 0, and approach linear behavior at high temperature. The Poisson ratio also behaves regularly, having a positive temperature coefficient. Between 295 and 4 K, elastic constants without a thermal-expansion correction change approximately 10 to 12% in E and G, and 4 to 5% in B and ν.
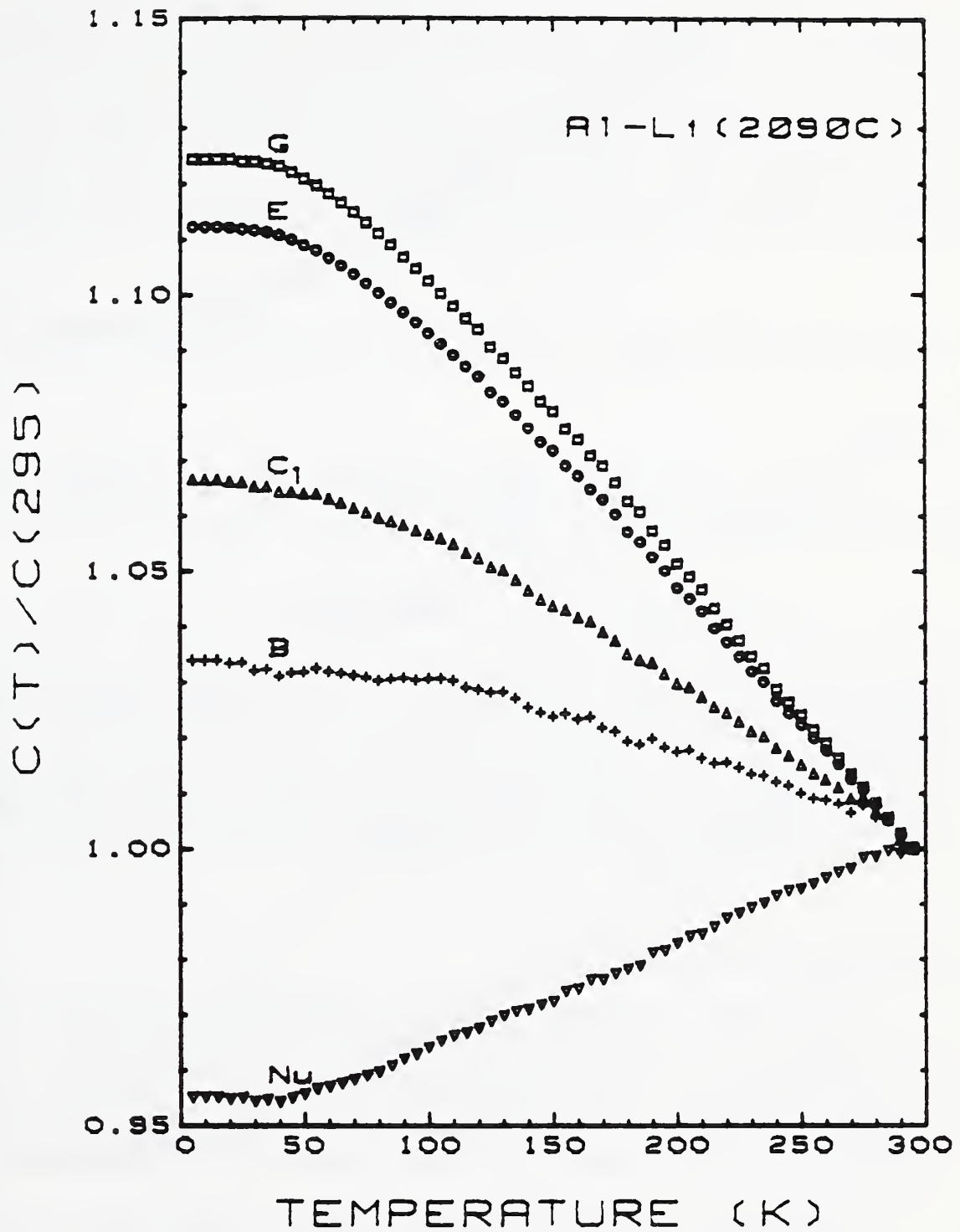
30

Fig. 13. Elastic properties (normalized to the room temperature value) vs. temperature for alloy 2090-3/4 with the specimen taken from the center of the plate thickness. The variation in properties with temperature is typical of all specimens tested in this program.

31

Section 3 -- THERMAL EXPANSION

Materials and Measurement Method

Thermal expansivity of seven different samples of the alloys was measured. The materials were the same as described in the elastic properties section (see Table 1). The change in length of each specimen between 4 and 320 K was measured with a quartz concentric tube dilatometer. Sample length was determined with a linear variable displacment transducer (LVDT) at 1 K intervals while temperature was monitored with a Type-E thermocouple placed inside the specimen. The entire apparatus was calibrated with standard OFHC copper. The coefficient of thermal expansion CTE (α) is normalized to the room temperature length L_o:

$$\alpha = (1/L_o) \cdot (dL/dT), \qquad (7)$$

where dL is the change in length for a given change in temperature dT in units of K.

Results

Figures 14 through 20 show data at 5° intervals plotted as $(L-L_o)/L_o$, where Lo is the sample length at 293 K. These points are fit to the function [8]

$$(L-L_o)/L_o = a + \frac{b}{(\exp(c/T)-1)}. \qquad (8)$$

Here a, b, and c are adjustable parameters relating to the alloys' physical properties and Einstein temperature. T is the sample temperature in Kelvin. The derivative of this function provides a smooth curve for the coefficient of thermal expansion. Both results are drawn with the raw data in Figs. 14-20, and tabulated results of the curve fits are shown at 10K intervals in Appendix B. Figures 21 and 22 show the results grouped by base material, and Fig. 21 compares our data for alloy 2219-T87 with Rhodes, et al. [9] data for 2219-T81 from 1963.

Discussion and Summary

A nth degree polynomial is often chosen for the fit of $(L-L_o)/L_o$. However, this function has no physical basis and exhibits large errors near the endpoints of the data set. The present function is chosen because of its relation to elastic properties, and is suitable for materials that show ordinary temperature dependence -- that is, zero slope at low temperature and a smooth monotonic increase to linear behavior at high temperature, with no phase transitions.

Analysis of the fit of thermal expansion data for high purity copper and aluminum to this function for calculating CTE shows that the difference between the measured data points and the curve is less than 5%. This is sufficient to account for the difference between samples of alloys 2090 and X2095 (Figs. 21 and 22).

32
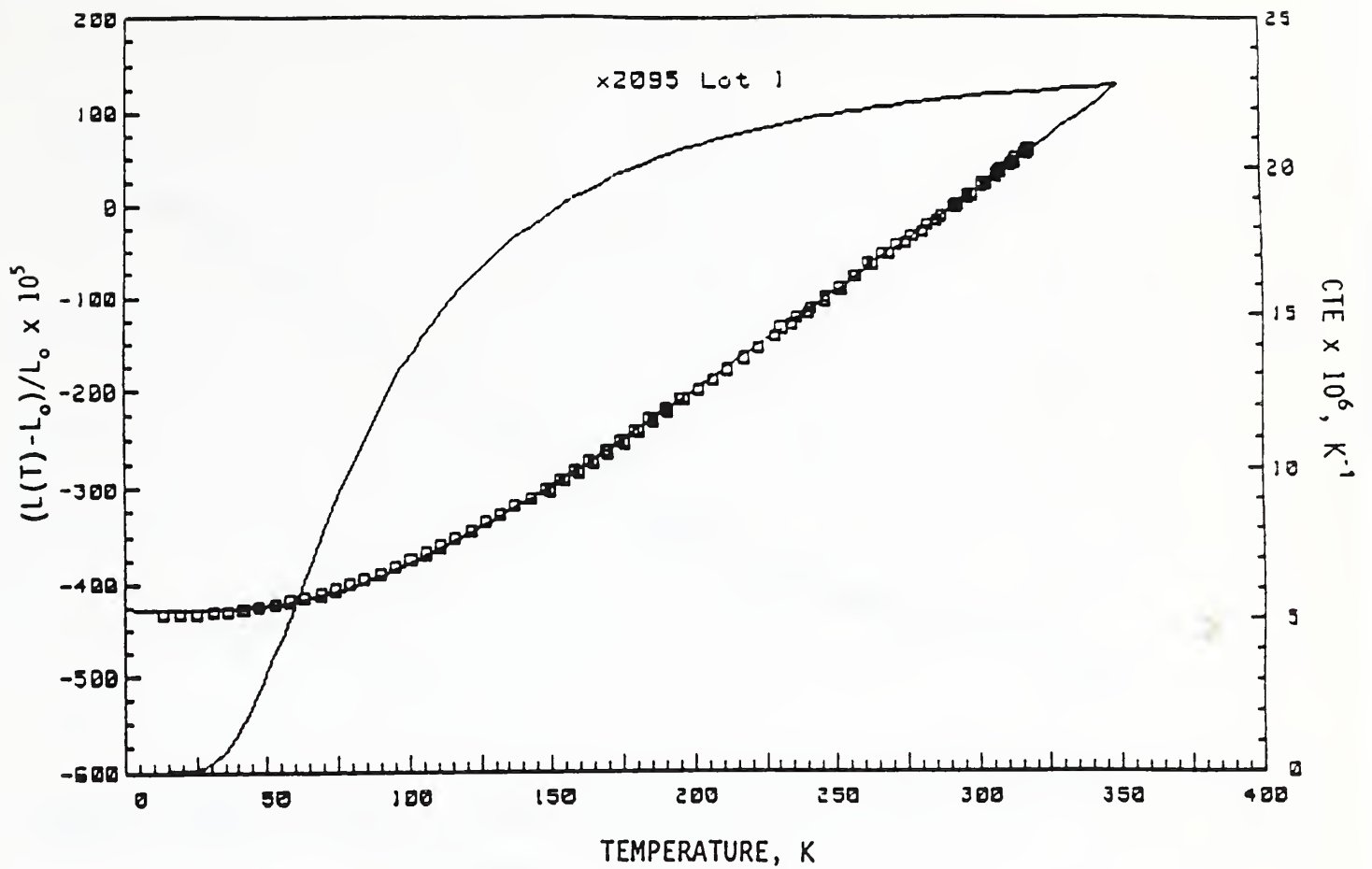
Fig. 14. ΔL/L$_o$ and CTE vs. temperature for alloy X2095 (lot 1).
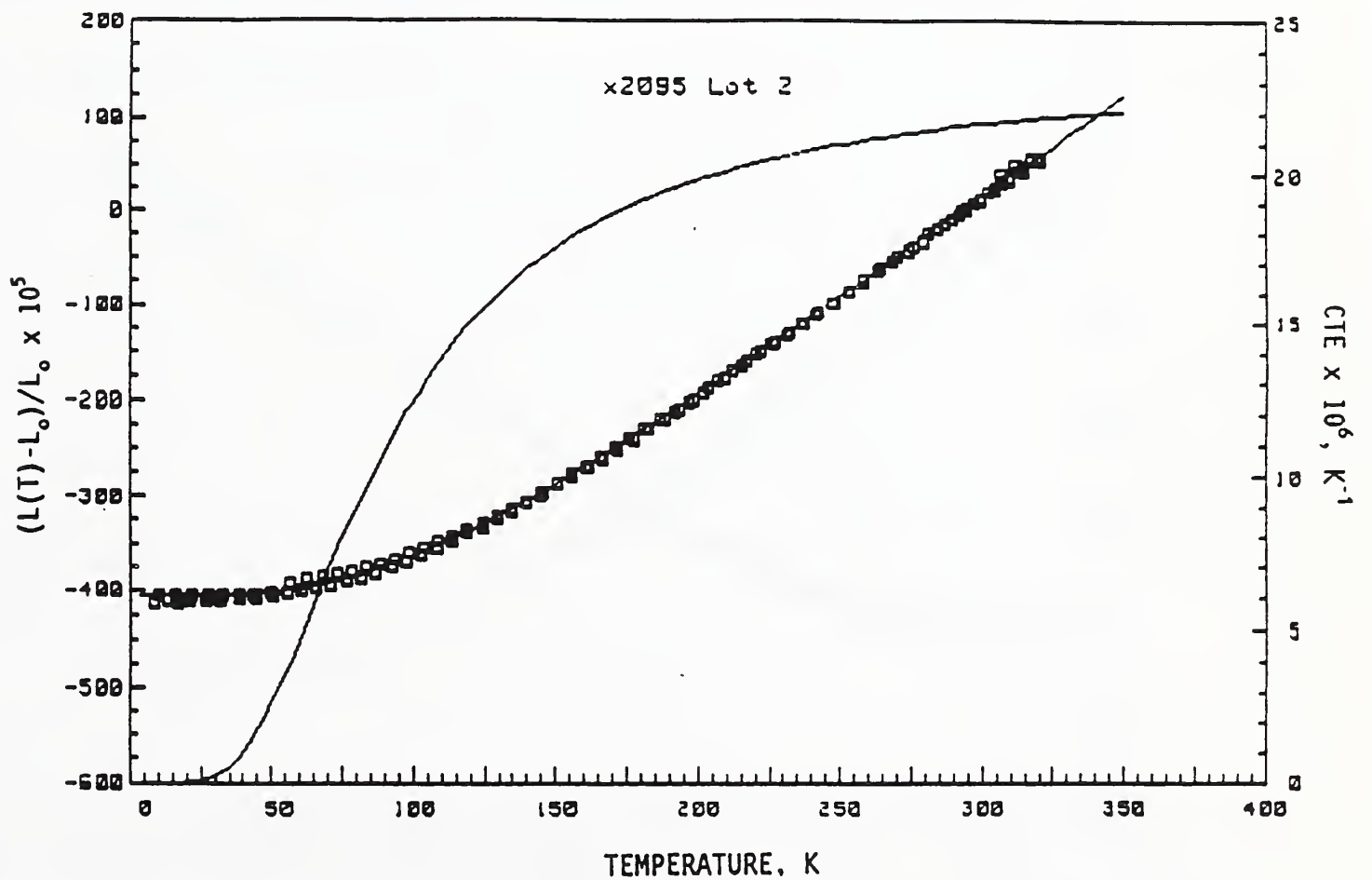
Fig. 15. ΔL/L$_o$ and CTE vs. temperature for alloy X2095 (lot 2).

33
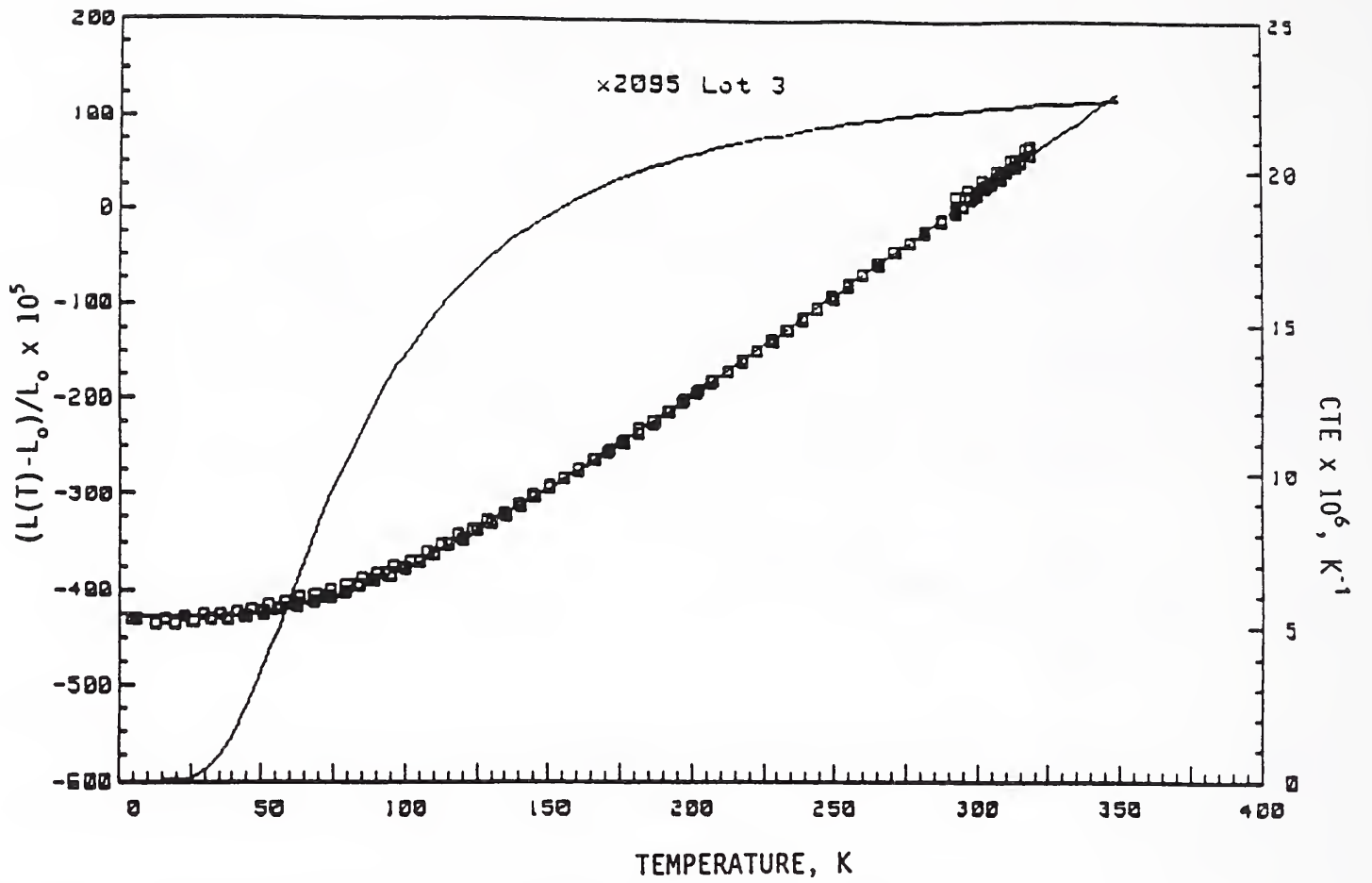
Fig. 16.   ▲L/L₀ and CTE vs. temperature for alloy X2095 (lot 3).
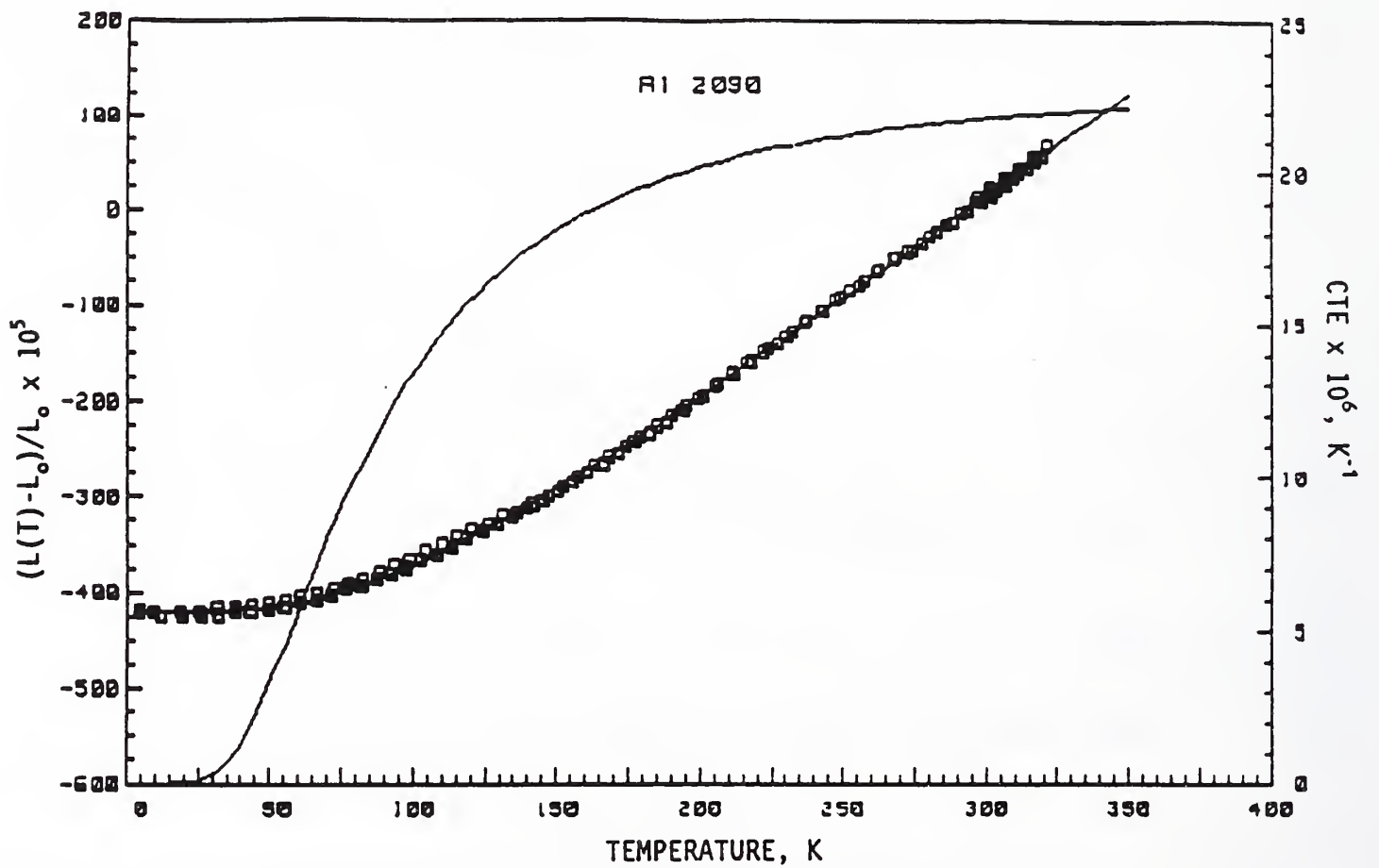
Fig. 17.   ▲L/L₀ and CTE vs. temperature for alloy 2090-T81 -1/2.

34
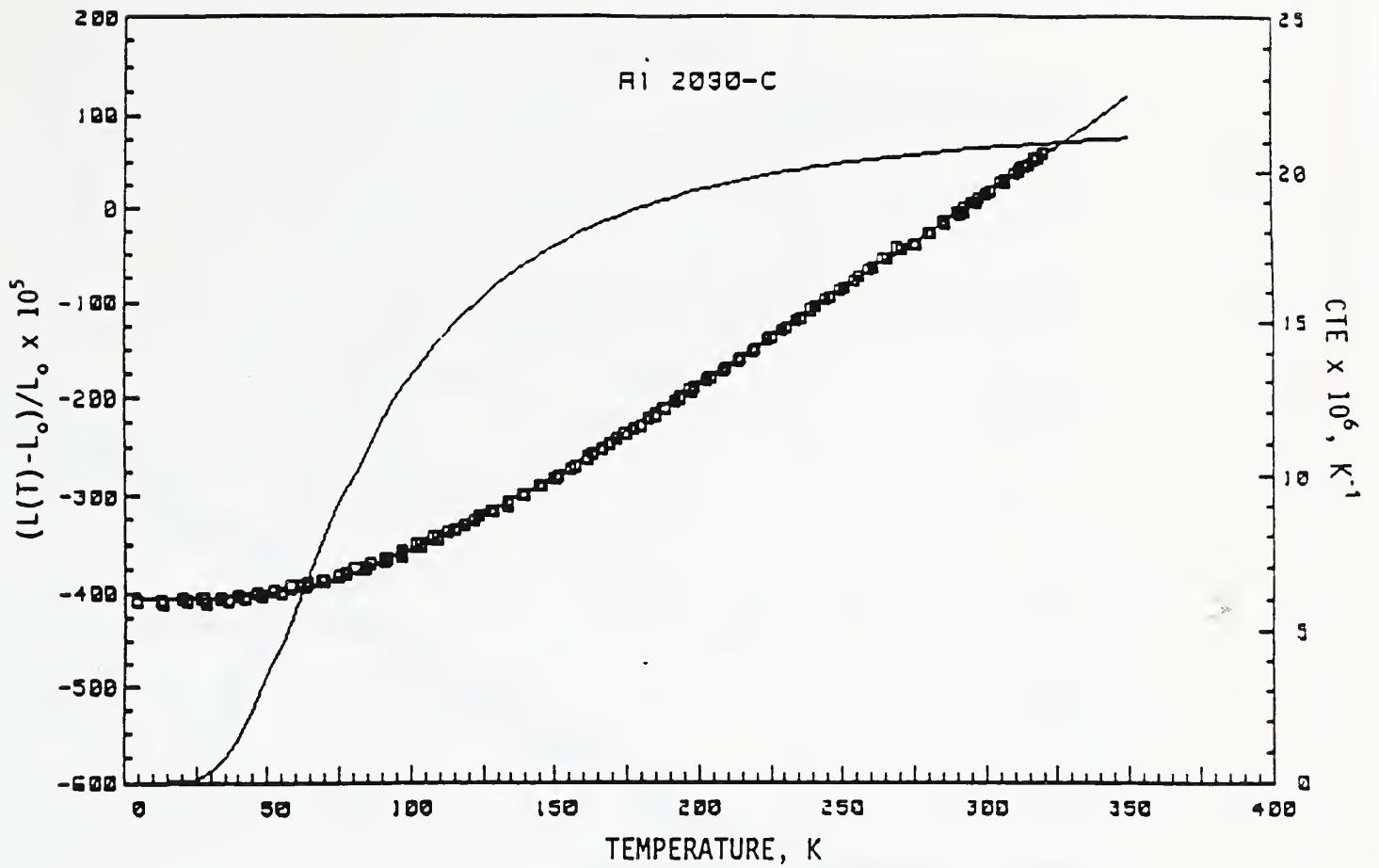
Fig. 18. ▲L/L$_o$ and CTE vs. temperature for alloy 2090-T81 -3/4 taken from the center of the plate.
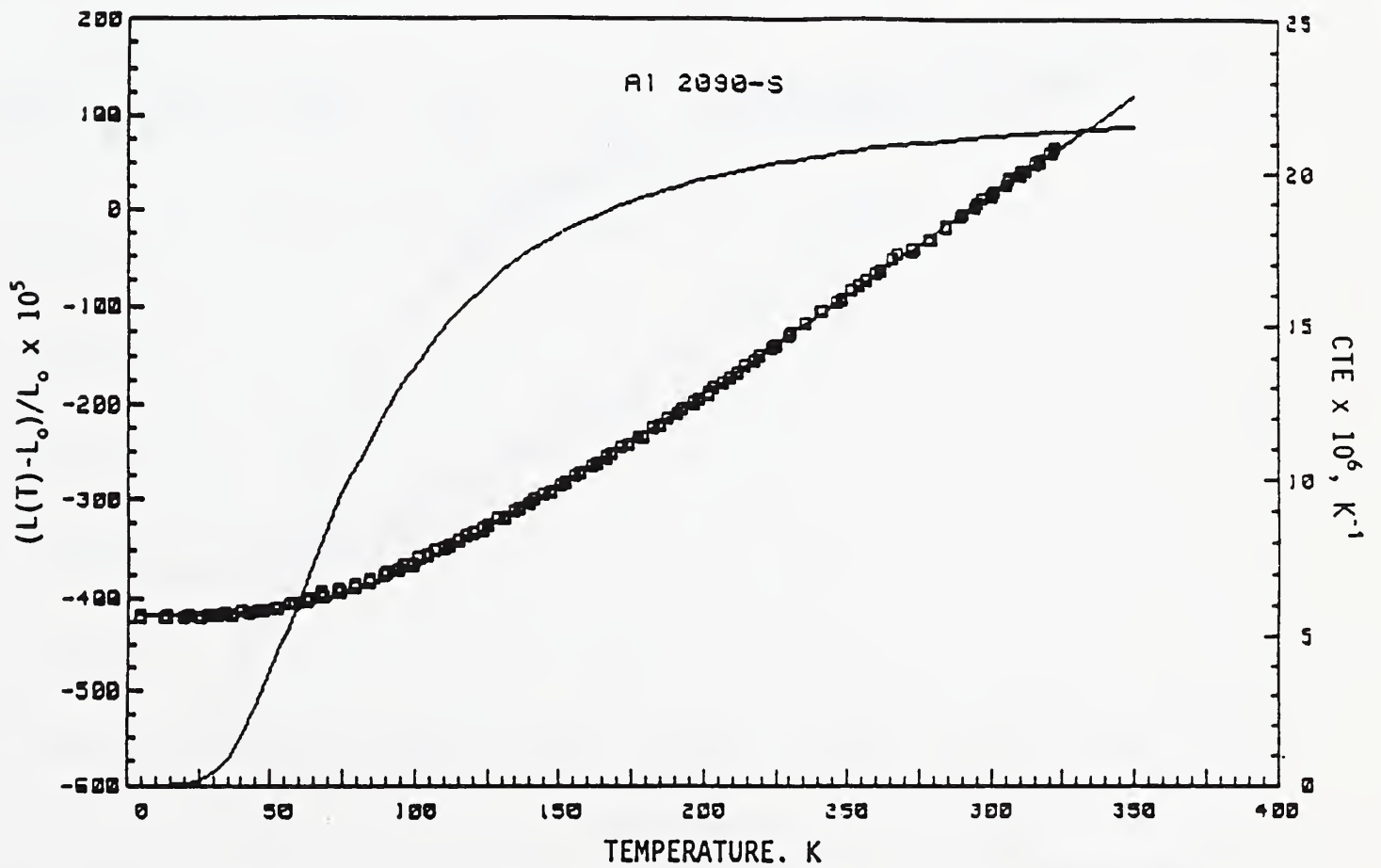
Fig. 19. ▲L/L$_o$ and CTE vs. temperature for alloy 2090-T81 -3/4 taken from the near-surface area of the plate.
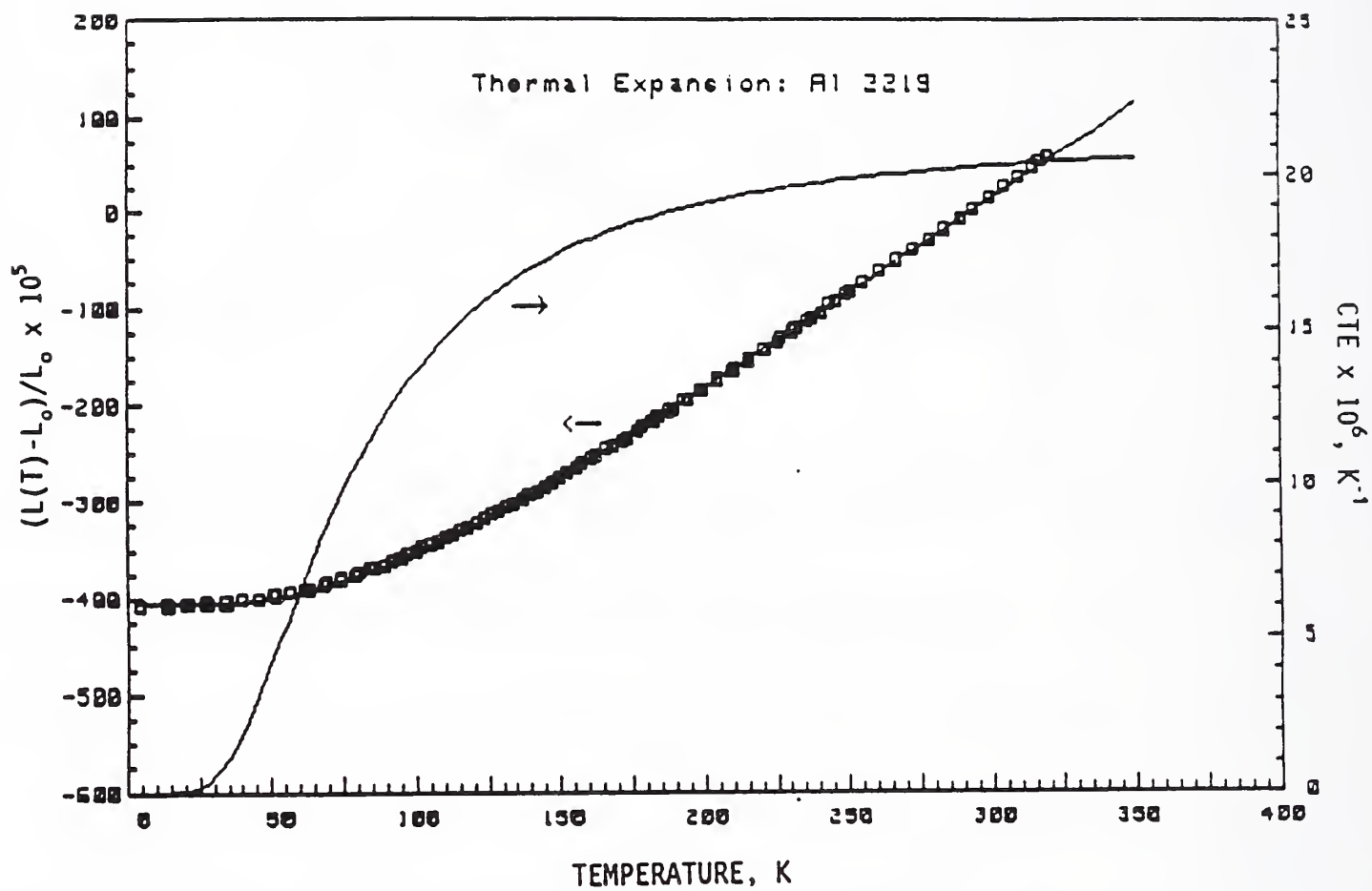
Fig. 20. $\Delta L/L_o$ and CTE vs. temperature for alloy 2219-T87.

36
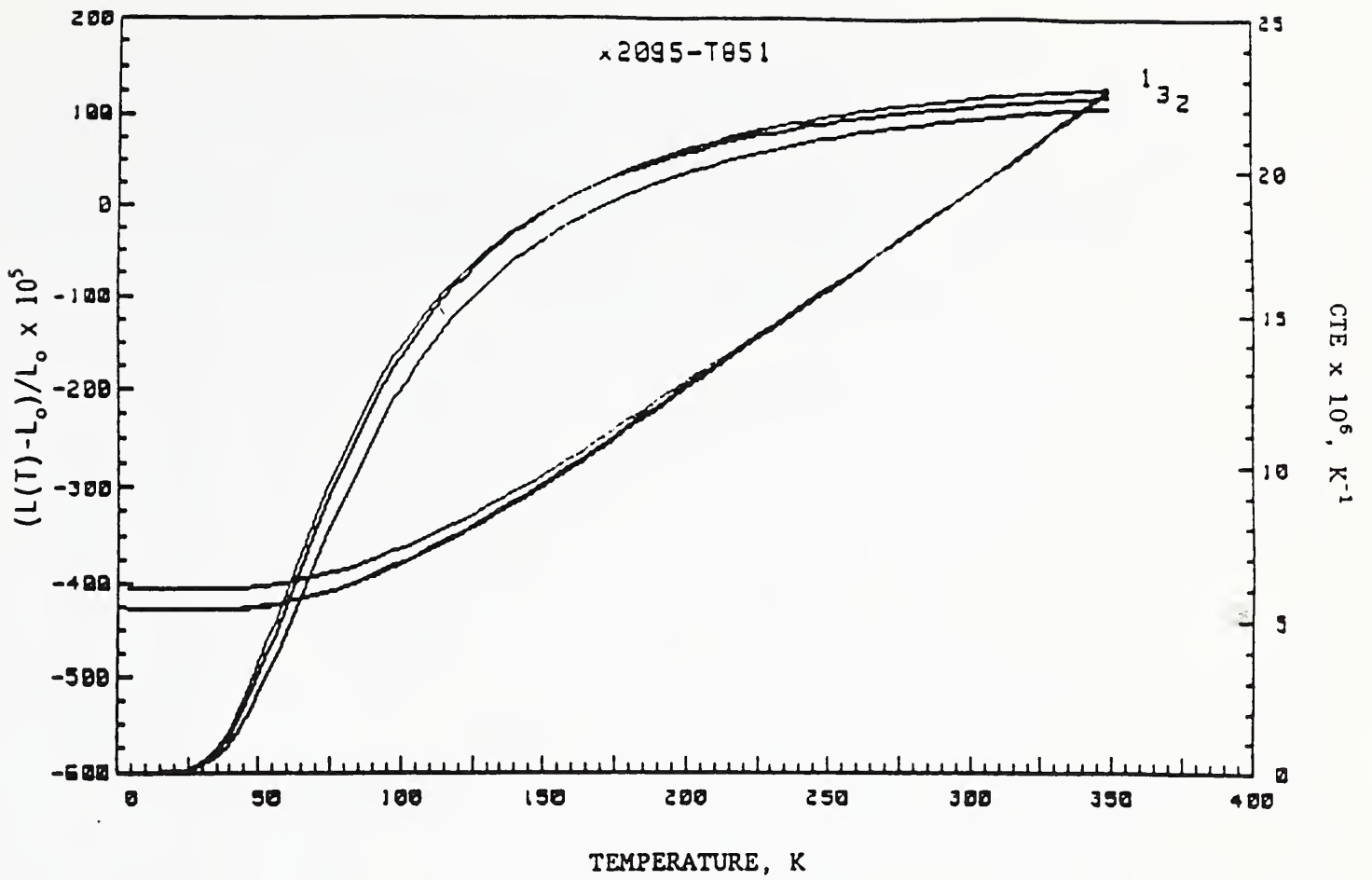
Fig. 21.   ΔL/L$_o$ and CTE vs. temperature for the three lots of alloy X2095.
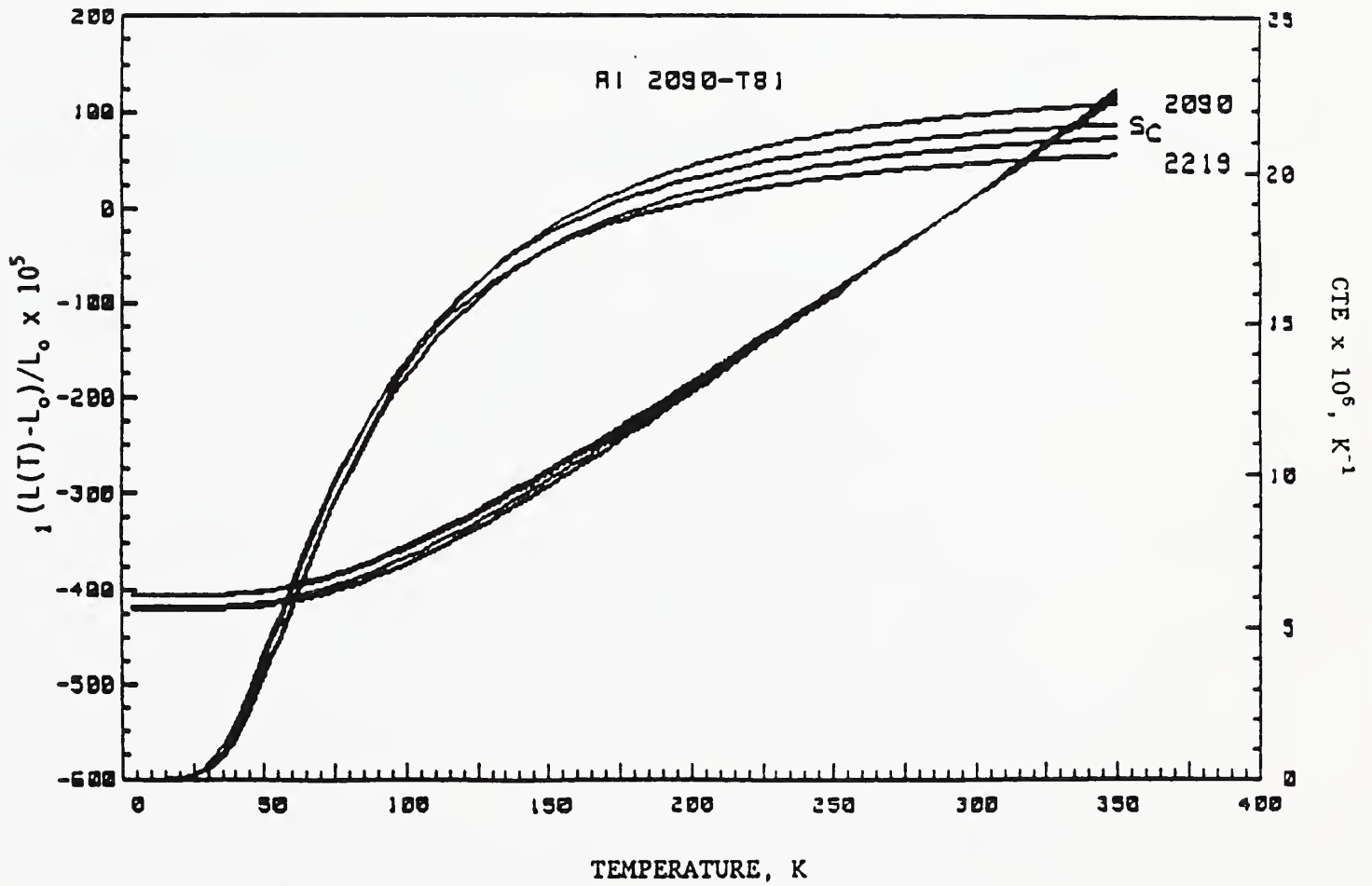
Fig. 22.   ΔL/L$_o$ and CTE vs. temperature for the three different specimens of alloy 2090.

The difference between the raw data for alloy 2219-T87 and Rhodes' data [9] for 2219-T81 is relatively small, yet the difference in CTE for the two sets of data is significant (see Fig. 23). The main reason for the deviation in CTE between today's material and that of three decades earlier is the data analysis procedure used. We choose this procedure because it is based on a theory with a physical basis rather than a strictly empirical approach.
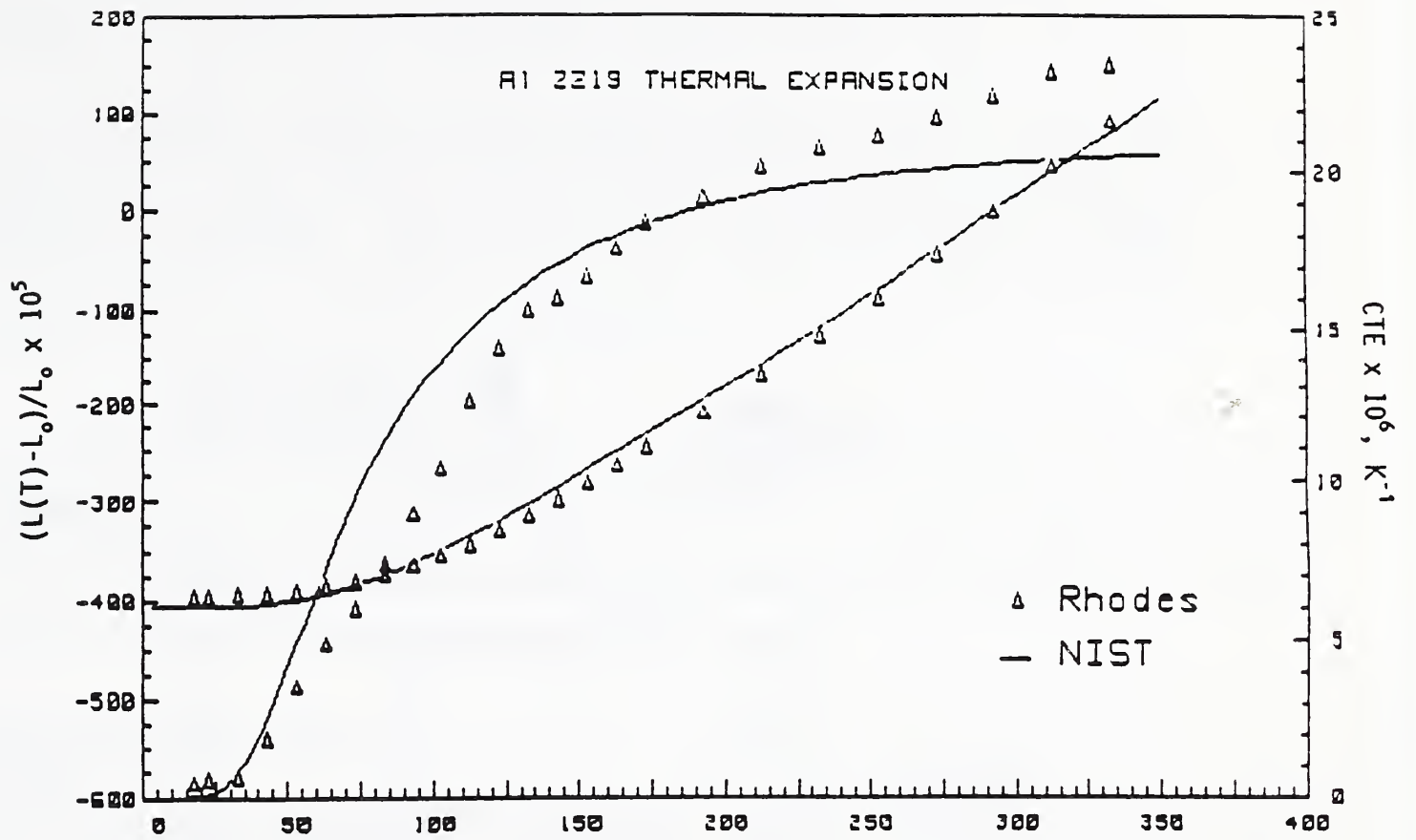
Fig. 23. $\Delta L/L_0$ and CTE vs. temperature for alloy 2219-T87 (1991) and for 2219-
T851 (1963).

39

Section 4 -- THERMAL CONDUCTIVITY

Apparatus

The apparatus used here to measure thermal conductivity is a previously described unguarded "fixed-point" apparatus [10], based on a method of axial one-dimensional heat flow. Some modifications have been made since the original publication appeared. The specimen chamber is shown schematically in Fig. 24. A specimen of known length and cross-sectional area is compressed between two isothermal copper blocks at controlled temperatures. Three stainless-steel bolts clamp the specimen between the two copper blocks; the flow of heat bypassing the specimen through the bolts is known and well characterized from previous calibration runs.
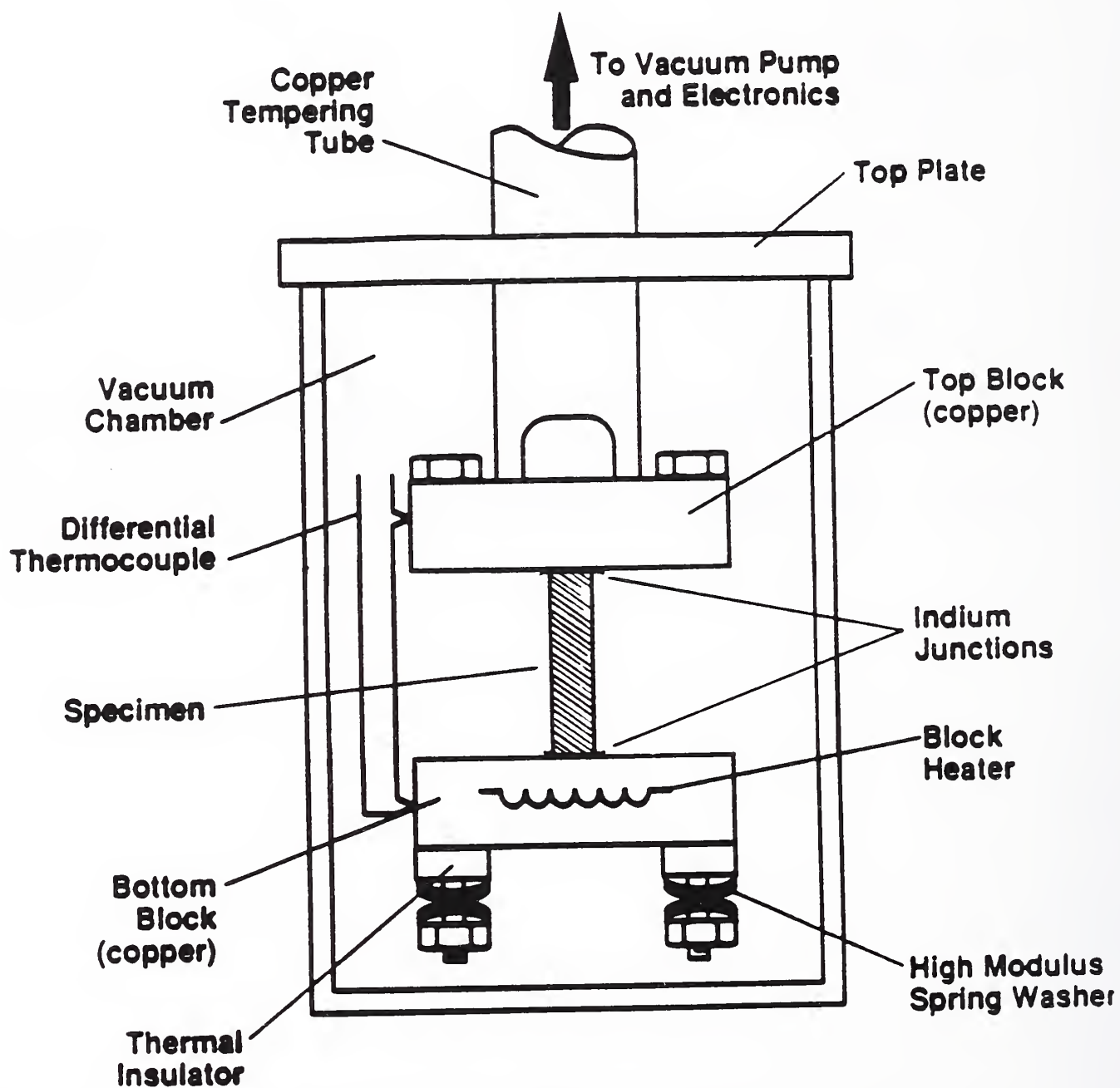
Figure 24.   Specimen chamber for fixed-point compression probe.

The upper, cooled, isothermal block is anchored to the top of the specimen chamber, which is usually immersed in one of four constant-temperature (fixed-point) baths. This upper block determines the cold-side temperature of the specimen. The nominal temperatures of these fixed-point baths are: 4 K (liquid helium), 76 K (liquid nitrogen), 194 K (a mixture of dry ice and alcohol), or 273 K (a mixture of pure ice and water).

The temperature of the lower, heated block is fixed by controlling the electric power supplied to its attached heater. This determines the hot-side temperature of the specimen, and establishes a fixed temperature difference across the specimen. Total power supplied to the hot block is determined from measurements of the voltage and current to its resistive heating element. Heat flowing through the specimen is computed by subtracting the calibrated heat flow through the compression bolts from the total power. For this Al-Li specimen, 88% to 94% of the total power flowed through the specimens.

AuFe-NiCr thermocouples are used to determine the cold-block temperature and the difference in temperature between the hot and cold blocks. The temperature differences established across the hot and cold blocks can be as much as 64 K. These temperature differences permit the use of different mean temperatures within the specimen subject to the constraint of the fixed cold-side temperatures. For this set of measurements, the maximum temperature difference maintained across the specimen was 47 K.

Experimental Procedure

Steady-state measurements were made with the specimen in a vacuum environment of 8×10^{-3} Pa (6×10^{-5} Torr) and with the specimen chamber in one of the fixed-point baths described earlier. The specimen had a 76 μm (0.003 in) indium foil and thermally conductive grease applied to the two contact surfaces between the specimen and the apparatus. The grease was used as a lubricant to prevent the indium foil from "cold welding" to the specimen and apparatus.

The specimen had a rectangular cross section 6.95 mm by 5.1 mm and a length of 25.4 mm. The specimen was clamped between the copper blocks by tightening the stainless steel bolts to 1.36 N·m (12 in·lb) of torque, applied at room temperature. This resulted in a compressive pressure on the specimen of approximately 121 MPa (17.5 ksi). The change in this load resulting from the cooling of the specimen to cryogenic temperatures, while not accurately known, is believed to be relatively small and did not affect the measurements of conductivity reported here. The use of indium-grease contacts coupled with enough contact pressure (above 90 MPa) is sufficient to permit the influence of thermal contact resistance to be neglected. After the specimen was compressed in the apparatus any additional excess grease and indium was removed.

<u>Computation of Thermal Conductivity</u>

Knowledge of the power Q_{spec} through the specimen, specimen geometry (length ℓ and cross-sectional area A) and temperature difference ΔT across the specimen allow the mean thermal conductivity, λ, to be calculated using the one-dimensional approximation of Fourier's law,

$$Q_{spec} = -\lambda \cdot A \cdot (dT/dx) \qquad (9)$$

recast into the approximate form

$$\lambda = (Q_{spec}/\Delta T) \cdot (\ell/A). \qquad (10)$$

Here the ratio $(\Delta T/\ell)$ in Eq. (10) approximates the derivative dT/dx in Eq. (9), and the conductivity obtained is the value averaged over the range of temperature defined by the temperature difference ΔT across the specimen.

When the thermal conductivity depends nonlinearly on temperature, as it does for these specimens, the larger values of temperature difference used during these measurements can introduce biases in the values of thermal conductivity calculated from Eq. (10). This is due to curvature of the conductivity function over the range of temperature ΔT. These biases were removed during analysis of the thermal conductivity data by use of an integral technique [11] which gives the correct functional dependence for the thermal conductivity.

<u>Results</u>

Thermal Conductivity of Alloy X2095 (4%Cu-1%Li):

The thermal conductivity of the alloy X2095 (4%Cu-1%Li) was measured over the temperature range 4.6 to 291 K. The experimental data are listed in Table 13. The function chosen to fit the thermal conductivity data is of the form

$$\lambda(T) = \sum_{i=1}^{n} a_i \, [\ell n \, (T+1)]^i. \qquad (11)$$

The resulting values of the six coefficients found to be sufficient to define the conductivity of this specimen are listed in Table 14. The thermal conductivity data for the aluminum–lithium alloy and the relative (percent) deviation of the data points from the fitted curve (Eqn. 10), are shown in Figs. 25 through 27. As is conventional, all conductivity data in the figures are plotted as a function of the (arithmetic) mean temperature of the specimen.

Figures 28 and 29 shows a comparison of the thermal conductivity for this aluminum-lithium alloy to that of other Al–Li alloys previously measured. Also included in the figures are conductivity measurements on the aluminum alloy 2219 for comparison.

42

Table 13. Experimental conductivity as a function of temperature for alloy X2095 specimen.

Temperature Difference, K	Average Temperature, K	Thermal Conductivity, W/(m·K)	Cold Bath
1	4.662	2.30	ℓHe
2	5.212	2.60	
4	6.355	3.20	
8	8.782	4.55	
16	14.039	7.47	
24	19.585	10.5	
32	25.293	13.5	
1	76.64	36.2	ℓN$_2$
2	77.29	36.4	
4	78.56	36.6	
8	81.14	37.3	
16	86.36	38.8	
24	91.68	40.2	
32	97.08	41.7	
46.9	107.38	44.4	
1	192.79	65.5	CO$_2$–alcohol
2	193.63	65.3	
4	195.22	65.0	
8	198.45	65.9	
16	205.10	68.5	
24	211.88	70.4	
28	215.40	71.3	
1	273.95	82.8	Ice–water
2	274.76	82.7	
4	276.37	83.1	
8	279.62	83.8	
16	286.18	85.0	
22.2	291.29	85.8	

Table 14. Coefficients of $\lambda(T)$ for alloy X2095 using Eqn. 10.

a_i	alloy X2095
1	-13.807958
2	25.800305
3	-17.443032
4	5.7295077
5	- 0.86399059
6	0.049828383
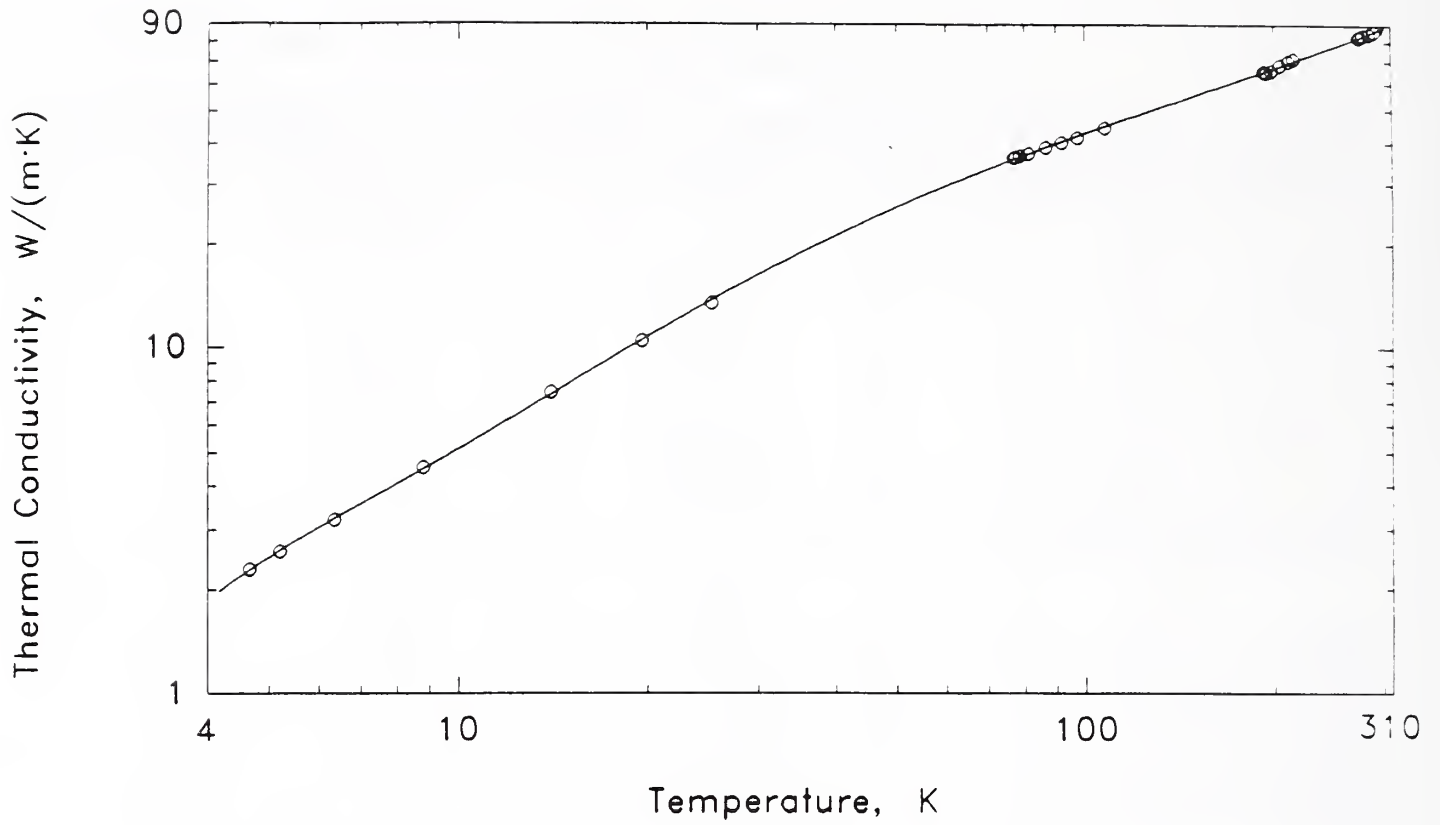
Fig. 25.   Thermal conductivity of alloy X2095 (4% Cu and 1% Li).   Experimental
data are represented as discrete points.   Both scales are logarithmic,
which clarifies the behavior at low temperatures.
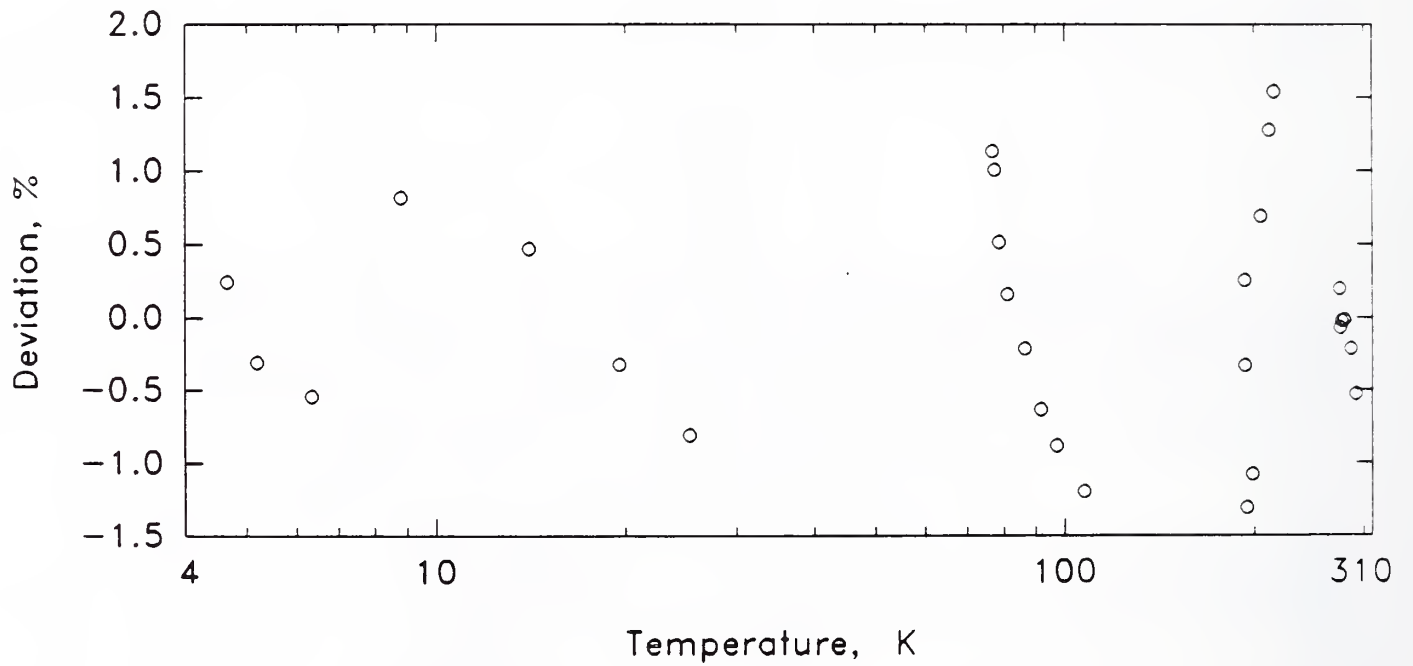
Fig. 26.   Relative deviations of the experimental and calculated thermal
conductivity for alloy X2095 (4% Cu and 1% Li).

44
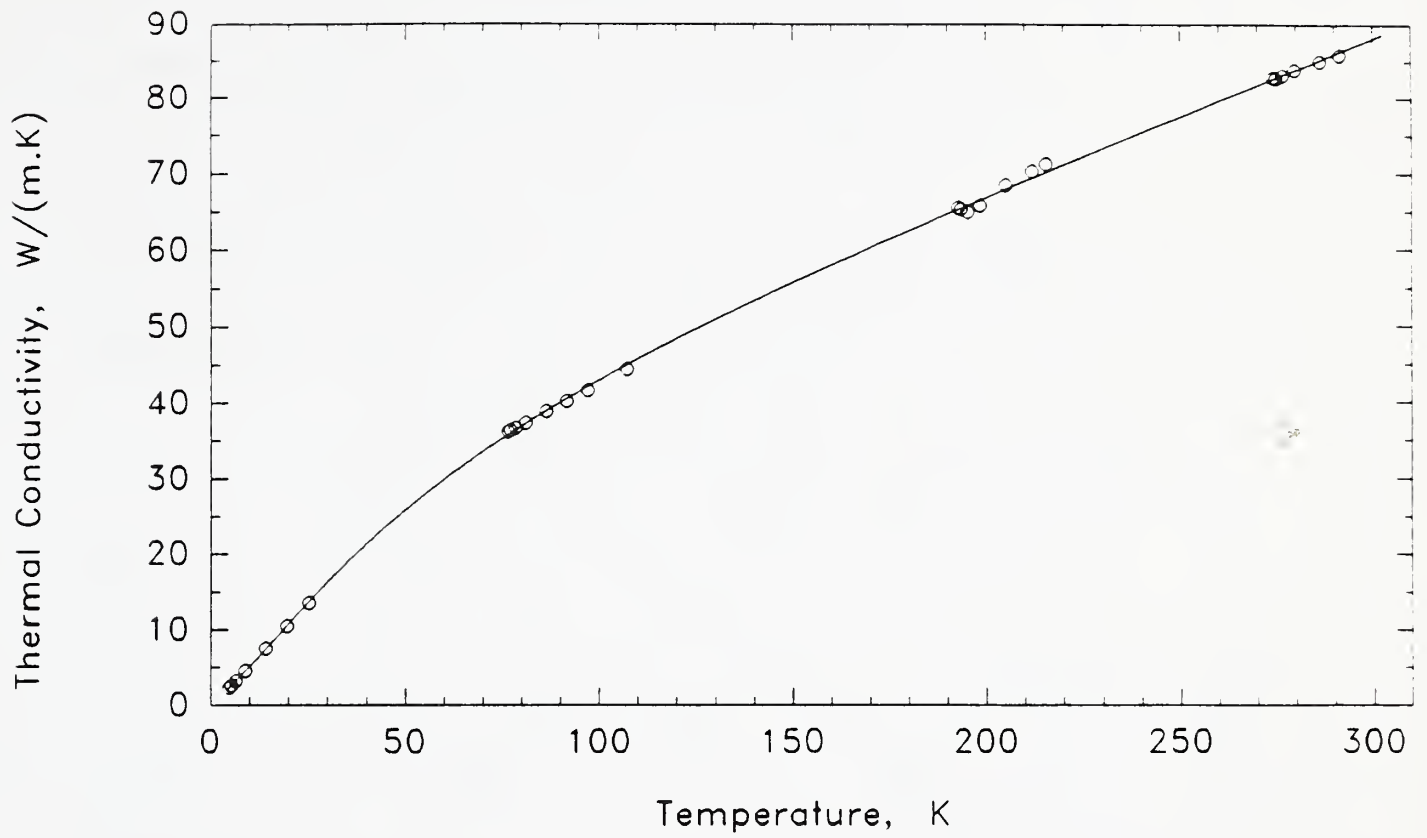
Fig. 27. Thermal conductivity of alloy X2095 (4% Cu and 1% Li). Experimental data are presented as discrete points. Both scales are linear, which clarifies the behavior at high temperatures.
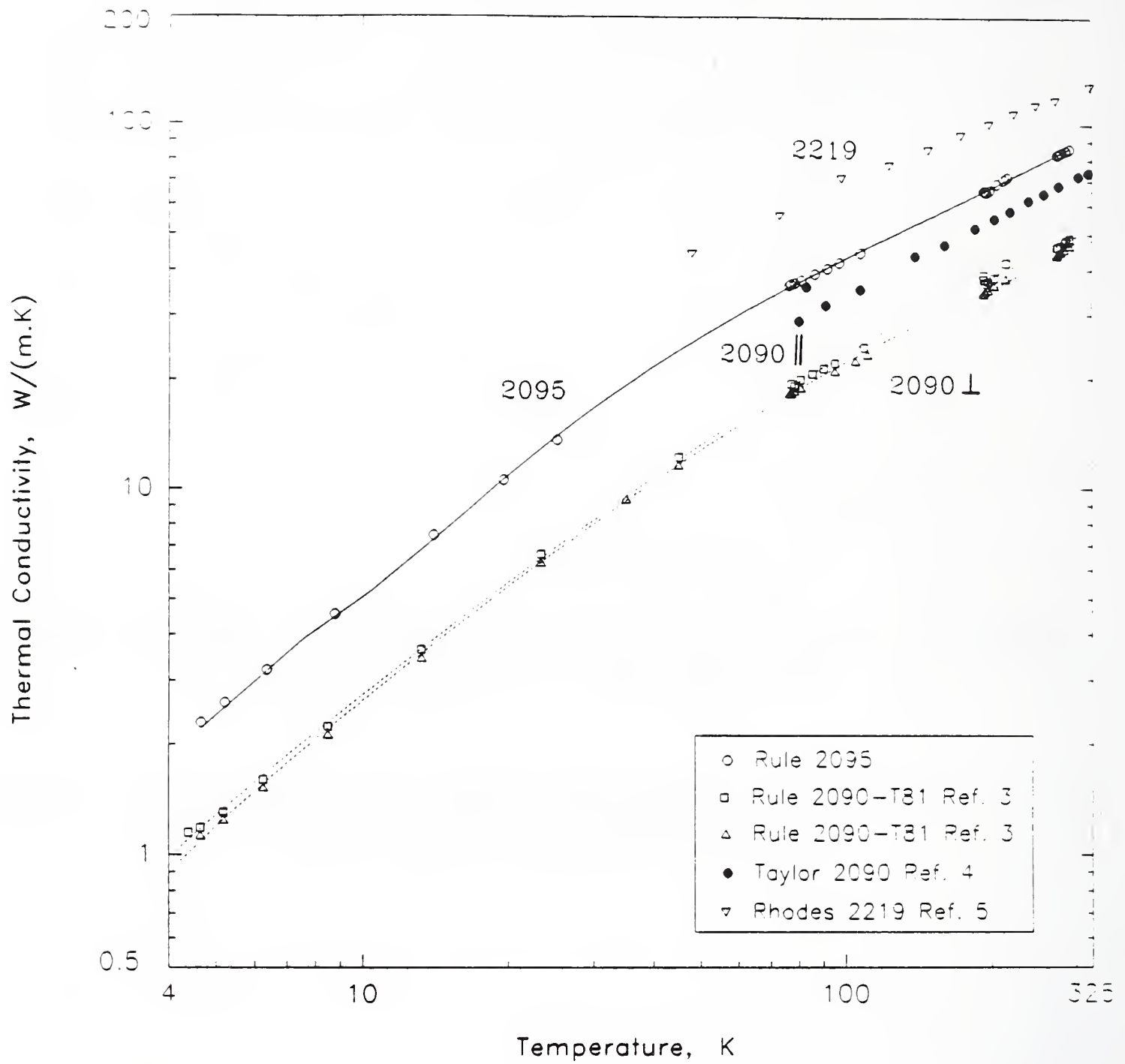
Fig. 28. Thermal conductivity of selected Al alloys from 4 to 325 K. Both scales are logarithmic which clarifies the behavior at low temperatures.
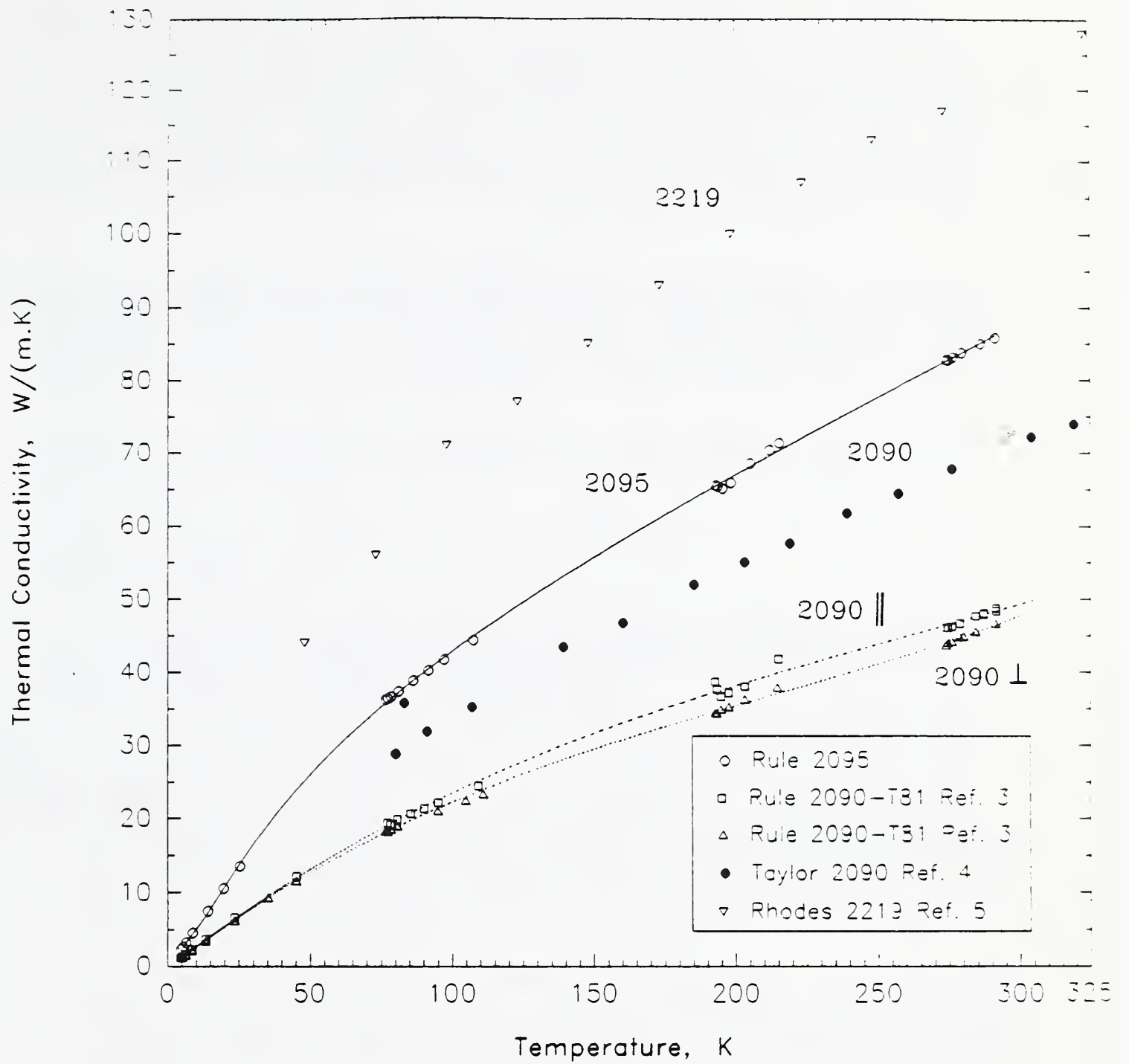
Fig. 29. Thermal conductivity of selected Al alloys from 4 to 325 K. Both
scales are linear which clarifies the behavior at high temperatures.

Previous measurements on the Al-Li alloy 2090 had significant variations in the results [1]. These studies involved similar specimens; however they utilized two different measurement techniques to determine the thermal conductivity. The conductivity differed by approximately 46% over the temperature range. Additional measurements of the electrical resistivity on the same specimens indicated that there were similar differences. Therefore there must be differences between the two specimens and not measurement techniques. Conductivity of aluminum alloys are very sensitive to variations in composition and cold-working of the material.

The conductivity of this aluminum-lithium alloy 2095 is 47% higher at 4.6 K and 77 K, and 43% higher at 300 K than the aluminum lithium alloy 2090 that was previously measured with this apparatus [1] and 23% at 77 K and 16% at 300 K from the other Al-Li 2090 data [12]. The conductivity of Al-Li alloy 2095 is 62% lower at 77 K and 41% lower at 300 K than the aluminum alloy 2219 [13].

Accuracy and reproducibility of measurements for moderate conducting material:

The accuracy of the original apparatus for moderate conducting material was ±10% [10]. After some modifications to the apparatus and automating the system, further tests on a stainless steel standard reference material (SRM 735) have indicated an overall system accuracy of ±5% (when measuring specimens having a conductivity similar to that of stainless steel). The accuracy of this apparatus for highly conductive materials has been studied by measuring the sintered tungsten SRM (8422). These measurements indicated the overall system accuracy to be ±8% when measuring highly conductive materials. Based on experience with this apparatus the imprecision has been found to be near 1% for a given specimen mounting and no more than ±5% for specimen remounting in the apparatus. Therefore the uncertainty of the results for this moderately conducting material, aluminum-lithium, is estimated to be ±6%. The maximum positive and negative deviations (Fig. 26) of the data from the fitted correlation is about 1.5 and 1.3 percent respectively.

OVERALL SUMMARY

The results of SCT testing have shown that the two Al-Li alloys have similar strength and toughness properties even though they fail by different mechanisms. Alloy 2090 generally has a better toughness ratio than alloy X2095. The results also show that the tensile properties can vary significantly, depending upon the location through the thickness of the plate. Clearly, more work needs to be done to understand the variation in mechanical properties through the thickness of plate products.

The physical and thermal properties of several Al-Li alloys have been measured as a function of temperature between liquid helium and room temperature. In general, these alloys behaved in a normal fashion and did not display any anamolous behavior or phase transitions. Li lowers the density, bulk modulus, and Poisson's ratio of the alloys while raising the shear and Young's modulus. The CTE vs. temperature curve displays a near zero slope near liquid helium temperature, increasing to a constant slope near room temperature. The thermal conductivity of alloy X2095 was lowest at liquid helium temperature, increased by a factor of 25 at 76 K, and was 37 times larger at room temperature.

ACKNOWLEDGEMENTS

REFERENCES

1. N.J. Simon, R.P. Reed, and E.S. Drexler, "Review of Mechanical and Physical Properties of Al-Li Alloys and Alloy 2219," report #AL-TR-90-064, Astronautics Lab (AFSC), Edwards AFB, CA and to be published as an NISTIR, Boulder, CO (1991).

2. R.P. Reed, P.T. Purtscher, N.J. Simon, J.D. McColskey, R.P. Walsh, J.R. Berger, E.S. Drexler, and R.L. Santoyo, "Aluminum Alloys for ALS Cryogenic Tanks: Comparative Measurements of Cryogenic Mechanical Properties of Al-Li Alloys and Alloy 2219," to be published as NISTIR 3979, Boulder, CO (1991).

3. ASTM E 740-88, "Standard Practice for Fracture Testing with Surface-Crack Tension Specimens," ASTM Book of Standards, American Society for Testing and Materials, Philadelphia, pp. 676-683 (1990).

4. W.T. Tack and L.W. Loechel, "Use of Applied Fracture Mechanics Principles to Evaluate the Cryogenic Fracture Toughness of Alloy 2090," submitted for publication in Al-Li conference proceedings, Garmisch, Germany, Oct. 1991.

5. Yi-Wen Cheng, R.B. King, D.T. Read, and H.I. McHenry, "Post-Yield Crack Opening Displacement of Surface Cracks in Steel Weldments," in <u>Fracture Mechanics: Fifteenth Symposium</u>, ASTM STP 833, R.J. Sanford, ed., American Society for Testing and Materials, Philadelphia, pp. 666-681 (1984).

6. NLS Huntsville Area Review Meeting, Nov. 19-20, 1991.

7. Y.P. Varshni, "Temperature Dependence of Elastic Constants," Phys. Rev. B, <u>2</u>, p.3952 (1970).

8. H. Ledbetter, "Thermal Expansion and Elastic Constants," Int. J. Thermophys., <u>12 (4)</u>, pp. 637-642 (1991).

9. B.L. Rhodes, C.E. Moeller, V. Hopkins, and T.I. Marx, "Thermal Expansion of Several Technical Metals from -255 to 300°C," in Advances in Cryogenic Engineering, Vol. 8, ed. K.D. Timmerhaus, Plenum Press, New York, pp. 278-286 (1963).

10. J.G. Hust and J. Arvidson, "Thermal Conductivity of Glass Fiber/Epoxy Composite Support Bands for Cryogenic Dewars," Internal Report No. 275.03-78-2, National Bureau of Standards, Boulder, Colorado (1978).

11. J.G. Hust and A.B. Lankford, "Comments on the Measurement of Thermal Conductivity and Presentation of a Thermal Conductivity Integral Method," Int. J. Thermophys. <u>3 (1)</u>, pp. 67-77 (1982).

12. R.E. Taylor, H. Groot, J. Larimore, "Thermal and Specific Heat of Aluminum-Lithium Alloy 2090," Thermophysical Properties Reesearch Laboratory, Purdue University, West Lafayette, Indiana, Report No. TPRL 878, 14 pp. (1989).

13. B.L. Rhodes, C.E. Moeller, and H.J. Sauer, "An Apparatus for Determining Thermal Conductivity of Solids from 20 to 600 K," Cryogenics, <u>5</u>, pp. 17-20 (1965).

APPENDIX A: TABLES OF PHYSICAL PROPERTIES
AS A FUNCTION OF TEMPERATURE

51

7 Oct 1991

Material:LiAl-2090

Temp(K)	Longitudinal Modulus(GPa)	Shear Modulus(GPa)	Bulk Modulus(GPa)	Young Modulus(GPa)	Poisson Ratio
295	112.7	30.40	72.18	79.97	0.3153
290	112.9	30.48	72.26	80.18	0.3150
280	113.4	30.65	72.58	80.61	0.3149
270	113.7	30.81	72.65	80.99	0.3142
260	114.1	30.98	72.82	81.40	0.3136
250	114.4	31.13	72.91	81.76	0.3130
240	114.7	31.27	73.06	82.10	0.3126
230	115.1	31.45	73.16	82.53	0.3119
220	115.4	31.62	73.30	82.95	0.3114
210	115.7	31.82	73.36	83.40	0.3105
200	116.0	31.96	73.44	83.73	0.3099
190	116.4	32.14	73.62	84.17	0.3094
180	116.6	32.30	73.59	84.54	0.3085
170	117.1	32.49	73.77	85.01	0.3079
160	117.4	32.64	73.87	85.35	0.3074
150	117.6	32.79	73.91	85.71	0.3067
140	117.9	32.93	74.03	86.04	0.3062
130	118.3	33.09	74.23	86.43	0.3059
120	118.5	33.24	74.26	86.79	0.3052
110	118.8	33.37	74.37	87.10	0.3048
100	119.0	33.51	74.40	87.42	0.3041
90	119.2	33.65	74.41	87.72	0.3035
80	119.4	33.77	74.38	88.01	0.3027
70	119.6	33.89	74.45	88.28	0.3023
60	119.8	33.99	74.49	88.52	0.3019
50	119.9	34.07	74.49	88.70	0.3015
40	119.9	34.14	74.44	88.85	0.3010
30	120.0	34.17	74.51	88.92	0.3011
20	120.1	34.18	74.60	88.96	0.3012
10	120.2	34.18	74.64	88.96	0.3013
5	120.2	34.18	74.64	88.96	0.3013

Recommended parameters:

Co:	120.11	34.181	74.544	88.942	0.3011
s:	-7.6382	-2.9778	-4.5512	-7.4143	0.009
t:	213.406	170.969	332.697	177.879	141.223

Equation:

$$C(T) = Co + s / (-1 + EXP (t / T))$$

52

7 Oct 1991

Material:LiAl-2095-W1

Temp(K)	Longitudinal Modulus(GPa)	Shear Modulus(GPa)	Bulk Modulus(GPa)	Young Modulus(GPa)	Poisson Ratio
295	113.1	28.78	74.73	76.52	0.3293
290	113.2	28.86	74.78	76.73	0.3239
280	113.6	29.04	74.89	77.15	0.3283
270	113.9	29.23	74.98	77.61	0.3274
260	114.2	29.38	75.10	77.99	0.3269
250	114.6	29.53	75.28	78.34	0.3265
240	114.9	29.70	75.31	78.77	0.3256
230	115.2	29.90	75.35	79.22	0.3247
220	115.6	30.06	75.51	79.63	0.3242
210	115.9	30.22	75.68	80.03	0.3237
200	116.3	30.38	75.79	80.41	0.3231
190	116.5	30.55	75.84	80.80	0.3224
180	116.8	30.71	75.90	81.18	0.3217
170	117.3	30.87	76.18	81.59	0.3215
160	117.6	31.03	76.26	81.97	0.3208
150	117.9	31.17	76.38	82.32	0.3203
140	118.3	31.35	76.53	82.75	0.3197
130	118.6	31.49	76.65	83.10	0.3193
120	118.8	31.62	76.67	83.39	0.3187
110	119.1	31.75	76.79	83.72	0.3183
100	119.4	31.91	76.88	84.10	0.3176
90	119.7	32.05	76.97	84.43	0.3171
80	119.9	32.11	77.14	84.61	0.3172
70	120.2	32.15	77.33	84.72	0.3174
60	120.4	32.26	77.44	84.98	0.3171
50	120.5	32.29	77.48	85.07	0.3170
40	120.7	32.30	77.69	85.10	0.3174
30	120.7	32.34	77.66	85.19	0.3171
20	120.7	32.34	77.67	85.19	0.3171
10	120.8	32.34	77.68	85.19	0.3172
5	120.8	32.34	77.68	85.19	0.3172

Recommended parameters:

Co:	120.82	32.339	77.737	85.189	0.3171
s:	-5.7252	-4.3742	-0.8078	-10.204	0.0274
t:	163.728	236.098	69.3536	229.254	344.947

Equation:

$$C(T) = Co + s / (-1 + EXP (t / T))$$

53

7 Oct 1991

Material:LiAl-2090C

Temp(K)	Longitudinal Modulus(GPa)	Shear Modulus(GPa)	Bulk Modulus(GPa)	Young Modulus(GPa)	Poisson Ratio
295	112.6	30.55	71.94	80.28	0.3140
290	112.8	30.63	72.01	80.49	0.3137
280	113.4	30.80	72.34	80.92	0.3135
270	113.6	30.96	72.40	81.30	0.3128
260	114.0	31.13	72.57	81.71	0.3123
250	114.3	31.28	72.66	82.07	0.3117
240	114.7	31.42	72.81	82.42	0.3113
230	115.0	31.60	72.91	82.84	0.3106
220	115.4	31.78	73.05	83.27	0.3100
210	115.7	31.97	73.11	83.72	0.3091
200	116.0	32.11	73.19	84.05	0.3086
190	116.4	32.29	73.37	84.49	0.3080
180	116.6	32.46	73.33	84.86	0.3071
170	117.0	32.65	73.51	85.33	0.3065
160	117.3	32.80	73.61	85.67	0.3060
150	117.5	32.95	73.65	86.03	0.3053
140	117.8	33.09	73.77	86.37	0.3048
130	118.3	33.25	73.96	86.75	0.3045
120	118.5	33.41	73.99	87.12	0.3037
110	118.8	33.54	74.11	87.43	0.3033
100	119.0	33.67	74.13	87.75	0.3027
90	119.2	33.81	74.14	88.05	0.3020
80	119.3	33.94	74.11	88.34	0.3013
70	119.5	34.05	74.18	88.61	0.3009
60	119.7	34.16	74.22	88.85	0.3005
50	119.8	34.24	74.22	89.03	0.3000
40	119.9	34.31	74.17	89.18	0.2995
30	120.0	34.33	74.24	89.25	0.2996
20	120.1	34.34	74.33	89.29	0.2997
10	120.1	34.34	74.37	89.30	0.2998
5	120.1	34.34	74.37	89.30	0.2998

Recommended parameters:

Co:	120.06	34.347	74.273	89.274	0.2997
s:	-7.6351	-2.9923	-4.5462	-7.4389	0.0091
t:	213.406	170.969	334.953	177.965	141.133

Equation:

$$C(T) = Co + s / (-1 + EXP (t / T))$$

54

7 Oct 1991

Material:LiAl-2090S

Temp(K)	Longitudinal Modulus(GPa)	Shear Modulus(GPa)	Bulk Modulus(GPa)	Young Modulus(GPa)	Poisson Rat:
295	112.4	30.62	71.63	80.41	0.3128
290	112.6	30.71	71.70	80.62	0.3126
280	113.2	30.88	72.03	81.05	0.3124
270	113.4	31.04	72.09	81.43	0.3117
260	113.8	31.21	72.26	81.84	0.3112
250	114.1	31.36	72.34	82.21	0.3106
240	114.5	31.50	72.49	82.55	0.3102
230	114.8	31.68	72.59	82.98	0.3094
220	115.2	31.86	72.73	83.40	0.3088
210	115.5	32.05	72.79	83.85	0.3080
200	115.8	32.19	72.87	84.18	0.3074
190	116.2	32.37	73.05	84.62	0.3069
180	116.4	32.54	73.01	84.99	0.3059
170	116.8	32.73	73.19	85.46	0.3053
160	117.1	32.88	73.29	85.81	0.3048
150	117.3	33.03	73.32	86.17	0.3041
140	117.6	33.17	73.44	86.50	0.3036
130	118.0	33.33	73.63	86.89	0.3033
120	118.3	33.49	73.67	87.25	0.3025
110	118.6	33.62	73.78	87.57	0.3021
100	118.8	33.76	73.80	87.88	0.3015
90	119.0	33.89	73.81	88.19	0.3008
80	119.1	34.02	73.78	88.47	0.3001
70	119.3	34.14	73.84	88.75	0.2996
60	119.5	34.24	73.89	88.98	0.2992
50	119.6	34.32	73.88	89.17	0.2988
40	119.6	34.39	73.83	89.32	0.2983
30	119.8	34.42	73.91	89.38	0.2984
20	119.9	34.43	73.99	89.43	0.2985
10	119.9	34.43	74.04	89.43	0.2986
5	119.9	34.43	74.04	89.43	0.2986

Recommended parameters:

Co:	119.83	34.432	73.938	89.411	0.2984
s:	-7.621	-2.9998	-4.5355	-7.4477	0.0092
t:	213.406	170.969	336.862	178.037	141.15

Equation:

$$C(T) = Co + s / (-1 + EXP (t / T))$$

55

7 Oct 1991

Material:LiAl-2219

Temp(K)	Longitudinal Modulus(GPa)	Shear Modulus(GPa)	Bulk Modulus(GPa)	Young Modulus(GPa)	Poisson Ratio
295	115.0	27.79	77.99	74.53	0.3407
290	115.1	27.86	77.99	74.70	0.3403
280	115.5	28.00	78.17	75.04	0.3399
270	115.8	28.14	78.28	75.40	0.3394
260	116.1	28.28	78.46	75.75	0.3390
250	116.4	28.42	78.53	76.10	0.3385
240	116.7	28.54	78.68	76.39	0.3381
230	117.0	28.66	78.80	76.68	0.3378
220	117.3	28.80	78.89	77.04	0.3372
210	117.6	28.95	79.06	77.42	0.3367
200	117.9	29.08	79.16	77.72	0.3363
190	118.1	29.22	79.19	78.07	0.3356
180	118.4	29.35	79.32	78.38	0.3353
170	118.7	29.51	79.44	78.79	0.3346
160	119.0	29.64	79.53	79.11	0.3342
150	119.3	29.78	79.64	79.46	0.3337
140	119.6	29.91	79.76	79.77	0.3333
130	119.9	30.04	79.85	80.08	0.3328
120	120.1	30.14	79.94	80.34	0.3325
110	120.4	30.23	80.10	80.57	0.3323
100	120.7	30.36	80.24	80.88	0.3320
90	120.8	30.42	80.27	81.03	0.3317
80	121.0	30.46	80.41	81.15	0.3318
70	121.2	30.53	80.51	81.32	0.3316
60	121.3	30.54	80.60	81.36	0.3317
50	121.4	30.60	80.64	81.49	0.3315
40	121.5	30.63	80.71	81.58	0.3315
30	121.6	30.65	80.77	81.63	0.3315
20	121.7	30.65	80.86	81.64	0.3317
10	121.6	30.66	80.76	81.65	0.3314
5	121.6	30.66	80.76	81.65	0.3314

Recommended parameters:

Co:	121.63	30.649	80.790	81.619	0.3315
s:	-6.6072	-4.0547	-1.5857	-9.807	0.0203
t:	205.264	259.191	133.705	254.911	338.554

Equation:

$$C(T) = Co + s / (-1 + EXP (t / T))$$

56

7 Oct 1991

Material:LiAl-2095-W2

Temp(K)	Longitudinal Modulus(GPa)	Shear Modulus(GPa)	Bulk Modulus(GPa)	Young Modulus(GPa)	Poisson Ratio
295	113.1	28.73	74.79	76.41	0.3297
290	113.2	28.81	74.85	76.62	0.3293
280	113.6	28.99	74.96	77.04	0.3287
270	113.9	29.18	75.05	77.50	0.3278
260	114.2	29.33	75.17	77.88	0.3273
250	114.6	29.47	75.35	78.23	0.3269
240	114.9	29.65	75.38	78.65	0.3261
230	115.2	29.85	75.42	79.11	0.3251
220	115.6	30.01	75.58	79.52	0.3246
210	115.9	30.17	75.75	79.91	0.3241
200	116.3	30.33	75.86	80.29	0.3235
190	116.5	30.49	75.91	80.68	0.3228
180	116.8	30.65	75.97	81.07	0.3221
170	117.3	30.81	76.26	81.47	0.3219
160	117.6	30.97	76.34	81.85	0.3212
150	117.9	31.11	76.46	82.20	0.3208
140	118.3	31.29	76.60	82.64	0.3202
130	118.6	31.44	76.73	82.98	0.3197
120	118.8	31.56	76.75	83.28	0.3191
110	119.1	31.69	76.87	83.60	0.3187
100	119.4	31.85	76.96	83.98	0.3181
90	119.7	31.99	77.04	84.31	0.3176
80	119.9	32.06	77.22	84.49	0.3176
70	120.2	32.09	77.41	84.60	0.3178
60	120.4	32.20	77.52	84.86	0.3175
50	120.5	32.24	77.56	84.95	0.3174
40	120.7	32.24	77.77	84.98	0.3178
30	120.7	32.28	77.74	85.07	0.3176
20	120.7	32.28	77.74	85.07	0.3176
10	120.8	32.28	77.75	85.07	0.3176
5	120.8	32.28	77.75	85.07	0.3176

Recommended parameters:

Co:	120.82	32.282	77.813	85.069	0.3175
s:	-5.7252	-4.3665	-0.8143	-10.194	0.0273
t:	163.728	236.098	69.6916	229.278	344.959

Equation:

$$C(T) = Co + s / (-1 + EXP (t / T))$$

57

7 Oct 1991

Material:LiAl-2095-W3

Temp(K)	Longitudinal Modulus(GPa)	Shear Modulus(GPa)	Bulk Modulus(GPa)	Young Modulus(GPa)	Poisson Rati
295	112.6	28.26	74.93	75.32	0.3324
290	112.7	28.34	74.99	75.53	0.3321
280	113.1	28.52	75.10	75.94	0.3314
270	113.4	28.70	75.19	76.40	0.3306
260	113.7	28.86	75.31	76.77	0.3301
250	114.1	28.99	75.49	77.12	0.3297
240	114.4	29.17	75.53	77.54	0.3289
230	114.7	29.36	75.57	77.99	0.3279
220	115.1	29.52	75.73	78.39	0.3274
210	115.4	29.68	75.90	78.78	0.3270
200	115.8	29.83	76.01	79.16	0.3264
190	116.0	30.00	76.06	79.54	0.3257
180	116.3	30.16	76.13	79.92	0.3250
170	116.8	30.31	76.42	80.32	0.3248
160	117.1	30.47	76.50	80.70	0.3241
150	117.4	30.61	76.62	81.04	0.3237
140	117.8	30.78	76.77	81.47	0.3231
130	118.1	30.92	76.89	81.81	0.3226
120	118.3	31.05	76.92	82.10	0.3220
110	118.6	31.18	77.04	82.42	0.3216
100	118.9	31.33	77.13	82.80	0.3210
90	119.1	31.47	77.22	83.13	0.3205
80	119.4	31.53	77.39	83.30	0.3206
70	119.6	31.57	77.58	83.41	0.3208
60	119.9	31.67	77.69	83.66	0.3205
50	120.0	31.71	77.74	83.75	0.3204
40	120.2	31.71	77.94	83.79	0.3203
30	120.2	31.75	77.91	83.87	0.3205
20	120.2	31.75	77.92	83.87	0.3205
10	120.2	31.75	77.93	83.87	0.3206
5	120.2	31.75	77.93	83.87	0.3206

Recommended parameters:

Co:	120.29	31.756	77.988	83.872	0.3205
s:	-5.7003	-4.2954	-0.8557	-10.079	0.0267
t:	163.728	236.098	71.9747	229.439	345.044

Equation:

$$C(T) = Co + s / (-1 + EXP (t / T))$$

58

APPENDIX B: TABLES OF THERMAL EXPANSION DATA
AS A FUNCTION OF TEMPERATURE

COEFFICIENT OF THERMAL EXPANSION OF Al 2090

Temp (K)	$10^5 \dfrac{L-Lo}{Lo}$	(CTE) $10^6 \dfrac{1}{(K)} \dfrac{1}{Lo} \dfrac{dL}{dT}$
5.00	-419.84	.00
15.00	-419.84	.00
25.00	-419.82	.07
35.00	-419.51	.70
45.00	-418.10	2.28
55.00	-414.75	4.48
65.00	-409.09	6.84
75.00	-401.13	9.05
85.00	-391.08	11.01
95.00	-379.21	12.67
105.00	-365.82	14.08
115.00	-351.13	15.26
125.00	-335.37	16.24
135.00	-318.70	17.07
145.00	-301.28	17.77
155.00	-283.20	18.36
165.00	-264.58	18.87
175.00	-245.49	19.30
185.00	-225.99	19.68
195.00	-206.15	20.01
205.00	-186.00	20.29
215.00	-165.58	20.54
225.00	-144.93	20.76
235.00	-124.07	20.96
245.00	-103.02	21.13
255.00	-81.81	21.28
265.00	-60.46	21.42
275.00	-38.97	21.55
285.00	-17.36	21.66
295.00	4.35	21.76
305.00	26.16	21.86
315.00	48.06	21.94

$$\frac{L-Lo}{Lo} = a + \frac{bc}{e^{c/T} - 1} ,$$

$$CTE(T) = \frac{bc^2 \, e^{c/T}}{(T(e^{c/T}-1))^2} , \quad \text{where} \quad \begin{aligned} a &= -419.84 \quad 10^{-5} \\ b &= 2.33 \quad 10^{-5} \\ c &= 264.1 \end{aligned}$$

60

COEFFICIENT OF THERMAL EXPANSION OF Al 2090-S

Temp (K)	$10^{-5} \dfrac{L-Lo}{Lo}$	(CTE) $10^{-5} \dfrac{1}{Lo} \dfrac{dL}{dT}$ (K)
5.00	-417.26	.00
15.00	-417.26	.00
25.00	-417.23	.10
35.00	-416.81	.91
45.00	-415.07	2.71
55.00	-411.21	5.05
65.00	-404.95	7.43
75.00	-396.42	9.60
85.00	-385.86	11.46
95.00	-373.60	13.02
105.00	-359.91	14.32
115.00	-345.04	15.39
125.00	-329.19	16.28
135.00	-312.53	17.03
145.00	-295.17	17.65
155.00	-277.25	18.18
165.00	-258.83	18.63
175.00	-240.00	19.02
185.00	-220.81	19.35
195.00	-201.31	19.64
205.00	-181.55	19.89
215.00	-161.54	20.11
225.00	-141.34	20.30
235.00	-120.95	20.47
245.00	-100.40	20.63
255.00	-79.70	20.76
265.00	-58.88	20.88
275.00	-37.94	20.99
285.00	-16.90	21.09
295.00	4.23	21.18
305.00	25.45	21.26
315.00	46.75	21.33

$$\frac{L-Lo}{Lo} = a + \frac{bc}{e^{c/T} - 1} \quad ,$$

$$CTE(T) = \frac{bc^2 \, e^{c/T}}{(T(e^{c/T}-1))^2} \quad , \text{ where}$$

$a = -417.26 \quad 10^{-5}$
$b = 2.25 \quad 10^{-5}$
$c = 249.73$

61

COEFFICIENT OF THERMAL EXPANSION OF x2095 Lot 1

Temp (K)	$10^5 \dfrac{L-L_o}{L_o}$	(CTE) $10^6 \dfrac{1}{L_o}\dfrac{dL}{dT}$ (K)
5.00	-428.01	.00
15.00	-428.01	.00
25.00	-427.99	.06
35.00	-427.71	.65
45.00	-426.37	2.18
55.00	-423.12	4.38
65.00	-417.55	6.76
75.00	-409.64	9.03
85.00	-399.58	11.04
95.00	-387.65	12.77
105.00	-374.13	14.24
115.00	-359.25	15.47
125.00	-343.25	16.50
135.00	-326.30	17.37
145.00	-308.55	18.11
155.00	-290.12	18.74
165.00	-271.11	19.27
175.00	-251.60	19.73
185.00	-231.66	20.13
195.00	-211.36	20.47
205.00	-190.73	20.78
215.00	-169.82	21.04
225.00	-148.66	21.28
235.00	-127.28	21.48
245.00	-105.70	21.67
255.00	-83.95	21.83
265.00	-62.04	21.98
275.00	-39.99	22.11
285.00	-17.82	22.23
295.00	4.47	22.34
305.00	26.86	22.44
315.00	49.34	22.53

$$\frac{L-L_o}{L_o} = a + \frac{bc}{e^{c/T} - 1} ,$$

$$CTE(T) = \frac{bc^2 \, e^{c/T}}{(T(e^{c/T}-1))^2} , \text{ where}$$

$a = -428.01 \quad 10^{-5}$

$b = 2.39 \quad 10^{-5}$

$c = 268.83$

62

COEFFICIENT OF THERMAL EXPANSION OF <2095 Lot 2

Temp (K)	$10^5 \dfrac{L-L_o}{L_o}$	(CTE) $10^6 \dfrac{1}{(K)} \dfrac{1}{L_o} \dfrac{dL}{dT}$
5.00	-406.11	.00
15.00	-406.11	.00
25.00	-406.10	.04
35.00	-405.90	.47
45.00	-404.88	1.72
55.00	-402.23	3.65
65.00	-397.50	5.84
75.00	-390.56	8.00
85.00	-381.55	9.97
95.00	-370.70	11.70
105.00	-358.25	13.17
115.00	-344.43	14.43
125.00	-329.45	15.49
135.00	-313.50	16.39
145.00	-296.71	17.16
155.00	-279.21	17.82
165.00	-261.11	18.38
175.00	-242.48	18.86
185.00	-223.41	19.28
195.00	-203.94	19.65
205.00	-184.13	19.97
215.00	-164.02	20.25
225.00	-143.64	20.50
235.00	-123.03	20.72
245.00	-102.21	20.92
255.00	-81.20	21.09
265.00	-60.03	21.25
275.00	-38.71	21.39
285.00	-17.25	21.52
295.00	4.32	21.64
305.00	26.01	21.74
315.00	47.81	21.84

$$\frac{L-L_o}{L_o} = a + \frac{bc}{e^{c/T} - 1} \quad,$$

$$CTE(T) = \frac{bc^2 \, e^{c/T}}{(T(e^{c/T}-1))^2} \quad, \text{ where}$$

$$a = -406.11 \times 10^{-5}$$
$$b = 2.33 \times 10^{-5}$$
$$c = 282.96$$

63

COEFFICIENT OF THERMAL EXPANSION OF x2095 Lot 3

Temp (K)	$10^5 \dfrac{L-Lo}{Lo}$	(CTE) $10^6 \dfrac{1}{(K)} \dfrac{dL}{Lo\ dT}$
5.00	-428.86	.00
15.00	-428.86	.00
25.00	-428.84	.08
35.00	-428.48	.79
45.00	-426.91	2.49
55.00	-423.29	4.80
65.00	-417.27	7.23
75.00	-408.90	9.48
85.00	-398.41	11.45
95.00	-386.11	13.11
105.00	-372.27	14.51
115.00	-357.16	15.68
125.00	-340.99	16.65
135.00	-323.92	17.46
145.00	-306.10	18.15
155.00	-287.65	18.73
165.00	-268.66	19.23
175.00	-249.22	19.66
185.00	-229.37	20.02
195.00	-209.19	20.34
205.00	-188.70	20.62
215.00	-167.96	20.86
225.00	-146.99	21.08
235.00	-125.81	21.27
245.00	-104.46	21.44
255.00	-82.94	21.59
265.00	-61.28	21.72
275.00	-39.50	21.85
285.00	-17.60	21.96
295.00	4.41	22.05
305.00	26.51	22.14
315.00	48.70	22.23

$$\frac{L-Lo}{Lo} = a + \frac{bc}{e^{c/T} - 1},$$

$$CTE(T) = \frac{bc^2\, e^{c/T}}{(T(e^{c/T}-1))^2}, \quad \text{where}$$

$a = -428.86 \quad 10^{-5}$
$b = 2.35 \quad 10^{-5}$
$c = 258.65$

64

COEFFICIENT OF THERMAL EXPANSION OF Al 2219

Temp (K)	10^{-5} $\frac{L-Lo}{Lo}$	(CTE) 10^{-6} $\frac{1}{(K)}$ $\frac{dL}{Lo \, dT}$
5.00	-405.57	.00
15.00	-405.57	.00
25.00	-405.54	.14
35.00	-405.01	1.09
45.00	-403.02	3.02
55.00	-398.83	5.39
65.00	-392.25	7.72
75.00	-383.48	9.78
85.00	-372.80	11.52
95.00	-360.54	12.96
105.00	-346.97	14.14
115.00	-332.33	15.11
125.00	-316.80	15.92
135.00	-300.54	16.59
145.00	-283.67	17.14
155.00	-266.28	17.61
165.00	-248.46	18.01
175.00	-230.27	18.35
185.00	-211.77	18.65
195.00	-193.00	18.90
205.00	-173.98	19.12
215.00	-154.76	19.31
225.00	-135.36	19.48
235.00	-115.80	19.63
245.00	-96.10	19.77
255.00	-76.27	19.89
265.00	-56.34	19.99
275.00	-36.29	20.09
285.00	-16.16	20.17
295.00	4.05	20.25
305.00	24.34	20.32
315.00	44.69	20.39

$$\frac{L-Lo}{Lo} = a + \frac{bc}{e^{c/T} - 1} \, ,$$

$$CTE(T) = \frac{bc^2 \, e^{c/T}}{(T(e^{c/T}-1))^2} \, , \text{ where}$$

$a = -405.57 \quad 10^{-5}$
$b = 2.14 \quad 10^{-5}$
$c = 238.64$

65

COEFFICIENT OF THERMAL EXPANSION OF Al 2090-C

Temp (K)	$10^5 \frac{L-L_o}{L_o}$	(CTE) $10^6 \frac{1}{(K)} \frac{dL}{L_o \, dT}$
5.00	-405.04	.00
15.00	-405.04	.00
25.00	-405.02	.08
35.00	-404.67	.79
45.00	-403.13	2.43
55.00	-399.62	4.64
65.00	-393.82	6.94
75.00	-385.81	9.06
85.00	-375.81	10.90
95.00	-364.10	12.46
105.00	-350.97	13.76
115.00	-336.66	14.84
125.00	-321.35	15.75
135.00	-305.21	16.51
145.00	-288.38	17.14
155.00	-270.96	17.68
165.00	-253.04	18.14
175.00	-234.69	18.54
185.00	-215.99	18.88
195.00	-196.96	19.17
205.00	-177.66	19.43
215.00	-158.12	19.65
225.00	-138.36	19.85
235.00	-118.42	20.03
245.00	-98.31	20.18
255.00	-78.06	20.32
265.00	-57.67	20.45
275.00	-37.17	20.56
285.00	-16.56	20.66
295.00	4.15	20.75
305.00	24.94	20.84
315.00	45.82	20.91

$$\frac{L-L_o}{L_o} = a + \frac{bc}{e^{c/T} - 1} \, ,$$

$$CTE(T) = \frac{bc^2 \, e^{c/T}}{(T(e^{c/T} - 1))^2} \, , \text{ where}$$

$a = -405.04 \quad 10^{-5}$
$b = 2.21 \quad 10^{-5}$
$c = 256.11$

66

BL-114A	U.S. DEPARTMENT OF COMMERCE	1. PUBLICATION OR REPORT NUMBER

4. TITLE AND SUBTITLE

Aluminum-Lithium Alloys: Surface-Cracked Tension Fracture Tests and Physical and Thermal Properties at Cryogenic Temperatures

5. AUTHOR(S)

P.T. Purtscher, M. Austin, S. Kim, and D. Rule

11. ABSTRACT (A 200-WORD OR LESS FACTUAL SUMMARY OF MOST SIGNIFICANT INFORMATION. IF DOCUMENT INCLUDES A SIGNIFICANT BIBLIOGRAPHY OR LITERATURE SURVEY, MENTION IT HERE.)

Surface-cracked tension fracture tests were conducted in the T-S orientation at 295, 76, and 4 K on two plate alloys (X2095-T851, plate thickness of 12.7 mm and 2090-T81, plate thicknesses of 12.7 and 19.1 mm). The cryogenic toughness to room temperature toughness ratio for alloy 2090 is generally higher than that found for alloy X2095. Both alloys have significantly lower tensile properties near the surface of rolled plate than in the center of the plate.

The physical properties of seven plate specimens were measured from liquid helium to room temperature. Three variations in chemical composition of alloy X2095, three different samples of alloy 2090, and a single sample of alloy 2219-T87 were included. The mass density of Al alloys decreases by 4% / mass % of Li. The influence of texture on elastic properties is considered minimal because there is less than 5% variation in elastic-stiffness in the Al-Li alloys. The shear and Young's moduli increase 3 to 4% / mass % Li. The bulk modulus and Poisson ratio decrease by 3% / mass % Li.

Thermal expansion between 4 and 320 K was measured on the same seven plate specimens included in the physical properties study. All of the materials showed a typical temperature dependence where the slope of the coefficient of thermal expansion (CTE) vs. temperature curve has a zero slope near absolute zero and a smooth monotonic increase to a constant slope near room temperature.

The thermal conductivity of alloy X2095 (4%Cu-1%Li) was determined over the temperature range 4.2 to 300 K using a steady-state apparatus. The conductivity at 290 K was approximately 40% higher than at 77 K and was 37 times that at 4.6 K. The thermal conductivity of alloy X2095 is approximately twice that of alloy 2090, previously measured in the same apparatus. Compared to that of a published literature value for alloy 2219, the thermal conductivity of alloy X2095 is about 65% lower than for alloy 2219.

12. KEY WORDS (6 TO 12 ENTRIES; ALPHABETICAL ORDER; CAPITALIZE ONLY PROPER NAMES; AND SEPARATE KEY WORDS BY SEMICOLONS)

aluminum-lithium alloys; cryogenic properties; elastic properties; fracture toughness; residual strength; thermal conductivity; thermal expansion